

REVIEW PAPER

Mercury Cadmium Telluride Photodiodes at the Beginning of the Next Millennium

Antoni Rogalski

Military University of Technology, 2 Kaliskiego St., 00-908 Warsaw, Poland

ABSTRACT

At present, efforts in infrared (IR) detector research are directed towards improving the performance of large electronically scanned arrays and to obtain higher operating temperature of detectors. Another aim is to make IR detectors cheaper and more convenient to use. Mercury cadmium telluride (*HgCdTe*) ternary alloy system maintains its privileged position in IR detector technology. In this paper, the recent progress in *HgCdTe* photovoltaic detectors is described from the historical point of view. Discussion is mainly on homojunction and heterojunction photodiodes and their applications in large focal plane arrays and two-colour detectors. Also, an outlook on near-future trends in IR technologies is presented.

Keywords: Infrared detectors, homojunctions, heterojunctions, *HgCdTe* photodiodes, read-out integrated circuits, focal plane arrays, two-colour detectors

1. INTRODUCTION

The World War II saw the origins of modern infrared (IR) detector technology. Recent success in applying IR technology to remote sensing problems has been made possible by the successful development of high performance IR detectors over the last five decades. Many materials have been investigated in the IR field. Observing the history of the development of the IR detector technology, a simple theorem can be stated¹. 'All physical phenomena in the range of about 0.1 eV–1.0 eV can be proposed for IR detectors'. Among these effects are: Thermoelectric power (thermocouples), change in electrical conductivity (bolometers), gas expansion (Golay cell), pyroelectricity (pyroelectric detectors), photon drag, Josephson effect

[(Josephson junctions, superconducting quantum interference devices (SQUIDs)], internal emission (*PtSi* Schottky barriers), fundamental absorption (intrinsic photodetectors), impurity absorption (extrinsic photodetectors), low dimensional solids [superlattice and quantum well (QW) detectors], different types of phase transitions, etc. Figure 1 gives approximate dates of significant development efforts for the materials mentioned. Interest has centred mainly on the wavelengths of the two atmospheric windows in the range 3 μm –5 μm and 8 μm –14 μm , though in recent years, there has been increasing interest in longer wavelengths stimulated by space applications.

In 1959, research by Lawson², *et al.* at the Royal Radar Establishment, Malvern, UK,

triggered the development of variable band gap $Hg_{1-x}Cd_xTe$ mercury cadmium telluride ($HgCdTe$) alloys, providing an unprecedented degree-of-freedom on IR detector design. Soon thereafter, working under a US Air Force contract³, the group led by Paul Kruse at the Honeywell Corporate Research Centre, Hopkins, Minnesota, developed a modified Bridgman crystal growth method for $HgCdTe$ and then reported both photoconductive and photovoltaic detectors operated in long wavelength IR (LWIR; $8 \mu m \leq \lambda_c \leq 12 \mu m$) spectral range⁴ at 77K.

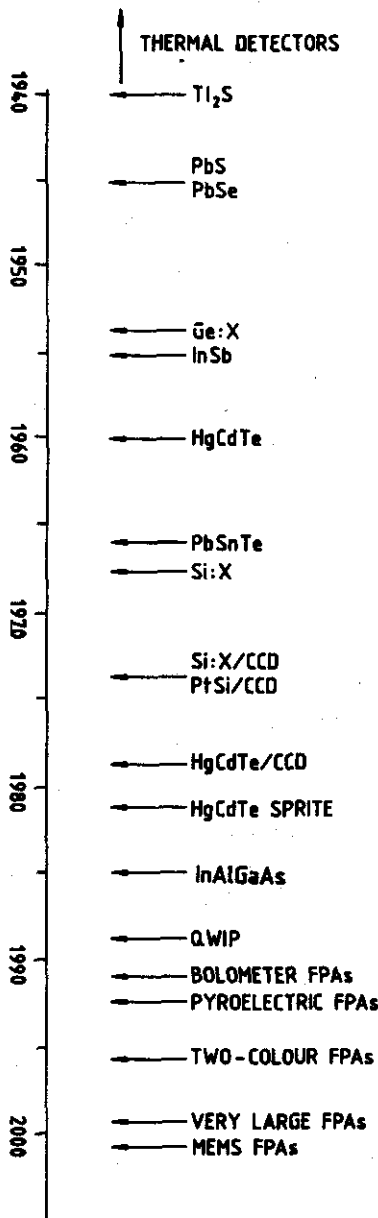


Figure 1. History of development of infrared detectors

$HgCdTe$ material technology development was, and continues to be, primarily for military applications. A negative aspect of support of defence agencies has been the associated security requirements that inhibit meaningful collaboration among research teams on a national, and especially international level. In addition, the primary focus has been on focal plane array (FPA) demonstration and much less on establishing the knowledge base. Nevertheless, significant progress has been made over four decades. The progress in $HgCdTe$ junction technology has been possible through important advances in various technologies: [maturation of liquid phase epitaxy (LPE), growth of complicated multilayer device structures by both molecular beam epitaxy (MBE) and metallo-organic chemical vapour deposition (MOCVD)] necessary to design and fabricate high performance FPAs and by understanding fundamental properties of $HgCdTe$ ternary alloy (donor and acceptor ion implantation mechanisms including the role of liberated mercury interstitials and the activation of arsenic from metal-sublattice to tellurium-sublattice). At present, $HgCdTe$ is the widely used variable gap semiconductor for IR photodetectors⁵. Over the years, it has successfully fought off major challenges from extrinsic silicon and $PbSnTe$ devices, despite that it has more competitors today than ever before. These include: Schottky barriers on silicon, $SiGe$ heterojunctions, $AlGaAs$ multiple QWs, $GaInSb$ strain layer SLs, high temperature superconductors, and especially two types of thermal detectors: Pyroelectric detectors and silicon bolometers. It is interesting, however, that none of these can compete in terms of fundamental properties. These may promise to be more manufacturable, but never to provide higher performance or, with the exception of thermal detectors, to operate at higher or even comparable temperatures.

In this paper, the current status and future trends in $HgCdTe$ detector technologies is presented considering an historical perspective of their developments. An overview of recent advances in photovoltaic $HgCdTe$ IR technology is presented. The focus is on *in situ* growth of band gap-engineered devices, such as buried-junction photodiodes and dual-band detectors. Finally,

anticipated evolution of IR technology in the next ten years is presented here.

2. *HgCdTe* TERNARY ALLOY FOR IR DETECTORS

The detectivity of an optimised IR photodetector of any type is limited by thermal processes in the active region of the device. This can be expressed as⁶

$$D^* = 0.31k \frac{\lambda}{hc} \left(\frac{\alpha}{G} \right)^{\frac{1}{2}} \quad (1)$$

where λ is the wavelength, h is Planck's constant, c is the light velocity, α is the absorption coefficient, G is the recombination rate, and $1 \leq k \leq 2$ is dependent on the contribution of recombination and backside reflection. As we can see, the ratio of absorption coefficient to the thermal generation rate, α/G , is the fundamental figure of merit of any material for IR photodetectors which directly determines the detectivity limits of the devices. Any potential material should be compared on this basis.

The main motivations to replace *HgCdTe* with alternative materials^{7,8} are the technological problems of this material. One of these is a weak *Hg-Te* bond, which results in bulk, surface and interface instabilities. Uniformity and yield are still issues. Nevertheless, *HgCdTe* remains the leading semiconductor for IR detectors. The important reasons for this are:

- None of the new materials offers fundamental advantages over *HgCdTe*. While the figure of merit, $(\alpha/G)^{1/2}$, of various narrow gap semiconductors seems to be very close to that of *HgCdTe*, the free carrier detectors and *GaAs/AlGaAs* SL devices have several orders of magnitude smaller α/G .
- *HgCdTe* exhibits extreme flexibility. It can be tailored for optimised detection at any region of IR spectrum, and dual and multicolour devices can be easily constructed.
- The relatively low dielectric constant ($\epsilon_s \approx 18\epsilon_0$) of *HgCdTe* (in contrast to those of lead

salts), permits low junction capacitance, that is important for fast response in laser pulse detectors and is also important for suppressing preamplifier noise below the detector noise in mid-wavelength (MW) ($3 \mu\text{m} \leq \lambda_c \leq 5 \mu\text{m}$) and short wavelength (SW) ($1 \mu\text{m} \leq \lambda_c \leq 3 \mu\text{m}$) photodiodes operating at low temperatures and low background fluxes (where the junction capacitance becomes an important contribution to the junction impedance at frequencies of interest).

- The present-day development of IR photodetectors has been dominated by complex band gap heterostructures. Among various variable band gap semiconductor alloys, *HgCdTe* is the only material, covering the whole IR spectral range, having nearly the same lattice parameter. The difference of lattice parameter between *CdTe* ($E_g = 1.5 \text{ eV}$) and *Hg_{0.8}Cd_{0.2}Te* ($E_g = 0.1 \text{ eV}$) is ≈ 0.2 per cent. Replacing small fraction of cadmium, with zinc or telluride with selenium (*Se*) can compensate the residual lattice mismatch. The independence of lattice parameter on composition is a major advantage of *HgCdTe* over any other material.

- The thermal expansion coefficient of *HgCdTe* is sufficiently close to that of silicon to allow hybrid arrangements of *HgCdTe* detector arrays and silicon multiplexer chips.

Actually, heterostructures do not offer inherent fundamental advantages over homo-structures for the conventional equilibrium mode devices. The fundamental limits to performance of IR detectors are imposed by unavoidable physics of optical and thermal generation in the narrow gap base region of a photodetector. Nevertheless, heterojunctions are helpful in achieving high performance in practice. For example, the narrow gap *HgCdTe* which absorbs IR radiation can be encapsulated in wider gap *HgCdTe* preventing instabilities due to the weak mercury-tellurium bonds. In addition, heterostructures can be used for nonequilibrium device whose potential performance can be much higher than that of the conventional ones⁹.

HgCdTe detectors are characterised by high optical absorption coefficient and quantum

efficiency and relatively low thermal generation rate compared to extrinsic detectors, silicide Schottky barriers and quantum well IR photodetectors (QWIPs). The operating temperature for *HgCdTe* detectors is, therefore, higher than for other types of photon detectors. In Fig. 2, plots of the calculated temperature required for background-limited performance (BLIP) operation in 30° field-of-view (FOV) are shown as a function of cut-off wavelength. *HgCdTe* detectors with BLIP operate with thermoelectric coolers in mid-wavelength infrared (MWIR) range, while the instead the low-wavelength infrared (LWIR) detectors operate at $\approx 100\text{K}$. The cooling requirements for QWIPs with cut-off wavelengths below 10 μm are less stringent in comparison with extrinsic detectors and Schottky barrier devices.

Epitaxy is the preferable technique to obtain device-quality *HgCdTe* epilayers for IR devices. The epitaxial techniques offer, in comparison with bulk growth techniques, the possibility to grow large area epilayers and sophisticated layered

structures with abrupt and complex composition and doping profiles, which can be configured to improve the performance of photodetectors. The growth is performed at low temperatures, which makes it possible to reduce the native defects density.

Epitaxial growth of the *HgCdTe* detector array on a silicon substrate, rather than *CdZnTe*, has emerged as a particularly promising approach to scale up wafer dimensions and achieve a cost-effective number of array dice from each processed wafer. In addition to the potential for increasing wafer size from the current 40 cm^2 for *CdZnTe* substrates to 150 cm^2 for silicon substrates, the growth of *HgCdTe* FPAs on silicon substrates offer other compelling advantages, such as creation of a thermal expansion-matched hybrid structure, superior substrate mechanical strength and flatness, elimination of impurity out-diffusion from the substrate, and compatibility with automated wafer processing and handling methodologies.

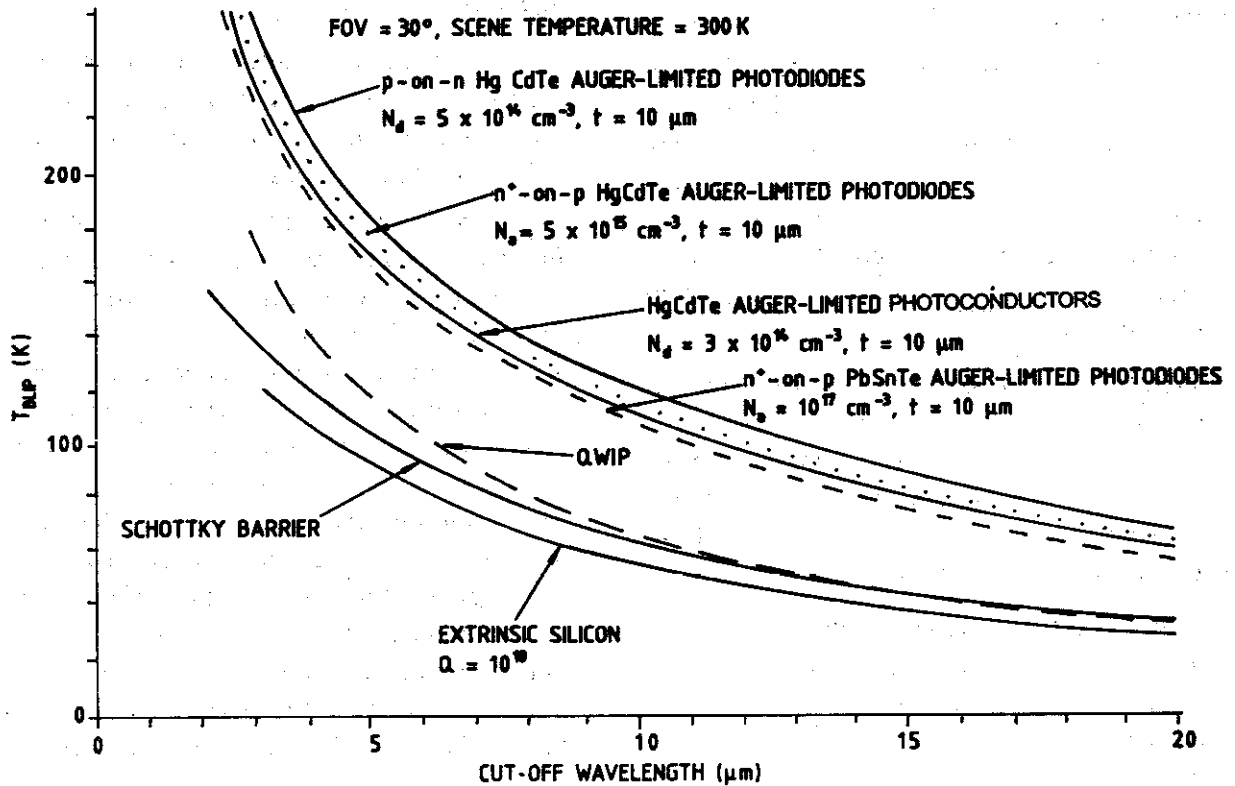


Figure 2. Estimation of temperature required for background-limited operation of different types of photon detectors. In the calculations, FOV = 30° and $T_B = 300\text{K}$ are assumed¹⁰.

Among the various epitaxial techniques, the LPE is the most matured method enabling growth of device-quality homogeneous layers and multilayered structures. LPE growth must be performed at relatively high growth temperature with consequent interdiffusion and resulting graded interfaces. The recent efforts are mostly on low growth temperature techniques like MOCVD and MBE. MOCVD is a nonequilibrium method, which appears to be the most promising for future large-scale and low-cost production of epilayers. The advantage of this method is the reduced growth temperature and the ability to modify the growth conditions to obtain required band gap and doping profiles. MBE offers unique capabilities in material and device engineering, including the lowest growth temperature, SL growth and potential for the most sophisticated composition and doping profiles. The growth temperature is $< 200\text{ }^{\circ}\text{C}$ for MBE but around $350\text{ }^{\circ}\text{C}$ for MOCVD, making it more difficult to control the *p*-type doping in the MOCVD due to the formation of mercury vacancies at higher growth temperatures. The main drawback of both these technologies is high cost of equipment and maintenance.

3. *HgCdTe* PHOTODIODE & FOCAL PLANE ARRAY ARCHITECTURES

The important application of *HgCdTe* photodiodes is in large 2-D electronically-scanned hybrid FPAs. Photodiodes with their very low power dissipation, easy multiplexing on focal plane silicon chip and less stringent noise requirements for the read-out integrated circuits (ROIC), can be assembled in 2-D arrays containing a very large ($\approx 10^6$) number of elements, limited only by existing technologies. A hybrid FPA consists of a 2-D photovoltaic detector array that is interfaced electrically, thermally and mechanically with a matching 2-D array of input circuits in a silicon complementary metal oxide semiconductor (CMOS) ROIC chip. Figure 3 shows the physical and electrical mating of a 2-D array of detectors to a silicon multiplexer, with individual interconnections between each detector and the

corresponding input to the multiplexer. Systems based upon such FPAs can be smaller, lighter with lower power consumption, and can result in much higher performance than systems based on first-generation detectors (e.g. the scanning systems which do not include multiplexing function in the focal plane). Photodiodes can also have less low frequency noise, faster response time, and the potential for a more uniform spatial response across each element. However, the complex processes needed for photovoltaic detectors have slowed down the development and the industrialisation of the second-generation systems, particularly for large arrays.

3.1 Hybrid Focal Plane Arrays

There are two types of hybrid *HgCdTe* FPAs shown in Fig. 3: (i) The backside illuminated indium bump-interconnected configuration, and (ii) the frontside illuminated loophole configuration. Each configuration requires fundamentally different photodiode design and processing.

A backside illuminated architecture utilises separately prepared detector arrays, which are then flipped over and hybridised to a silicon fanout pattern by means of indium bumps. A high optical fill factor is easily achieved with this technique. Two hybridisation techniques are in use. In one of the techniques, indium bumps are formed on both the *HgCdTe* detector array and the ROIC chip. The array and the ROIC chip are aligned and force is applied to cause the indium bumps to cold-weld together. In the other approach, indium bumps are formed only on the ROIC chip; the *HgCdTe* detector array is brought into alignment and proximity with the ROIC, the temperature is raised to cause the indium to melt, and contact is made by reflow. Backside illumination is readily achieved by the epitaxial growth of *HgCdTe* on transparent substrates, such as *CdTe*, *CdZnTe*, sapphire or silicon. No thinning of the material after hybridisation is required and the superior quality of epitaxial layers compared to bulk crystals is an additional advantage of this technique. With appropriate thermomechanical packing, the thermal

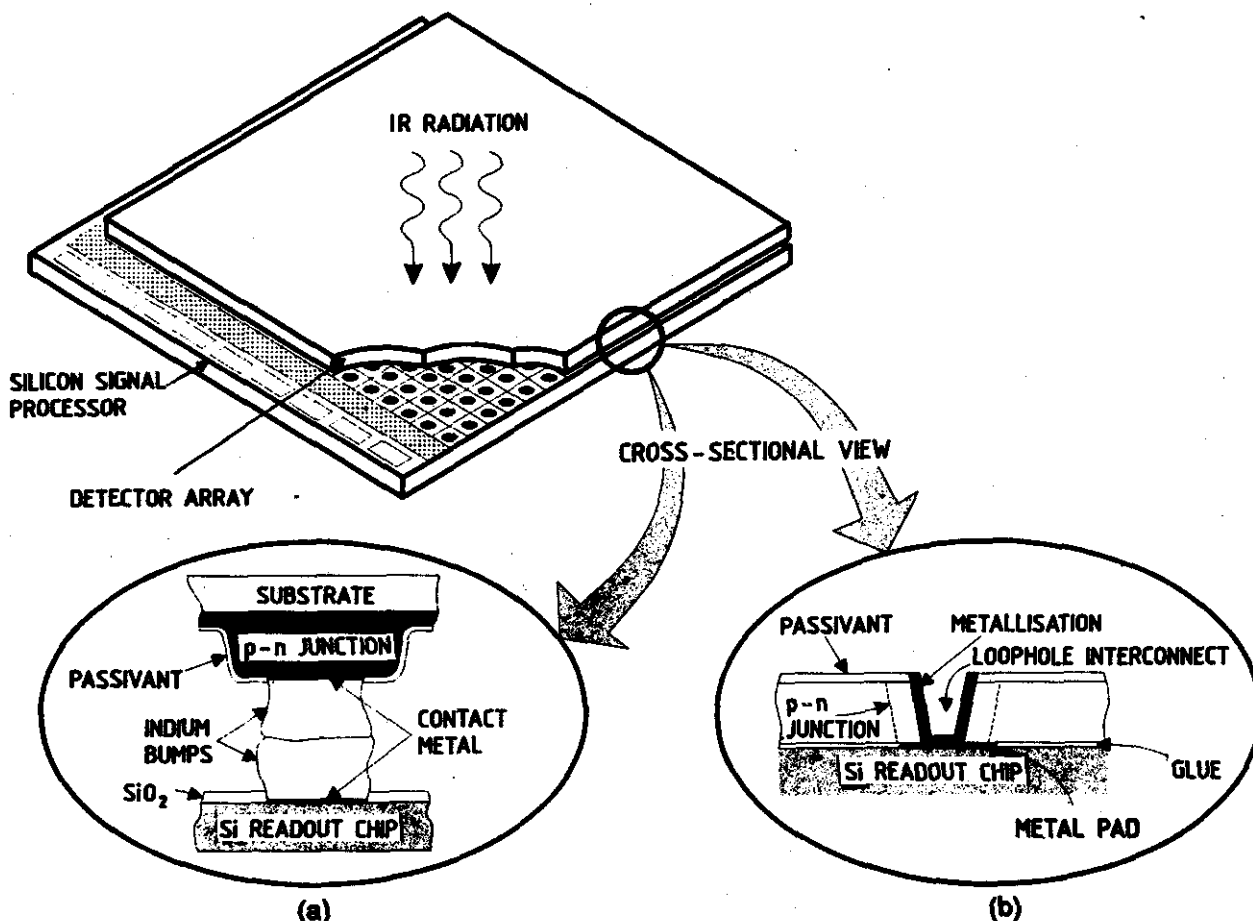


Figure 3. Hybrid $HgCdTe$ FPAs with independently optimised signal detection and read-out: (a) Indium bump technique, and (b) loop-hole technique.

expansion of a thinned silicon ROIC chip can be forced to match that of $HgCdTe$, so that there is negligible strain built up in the $HgCdTe$ detectors or indium bumps when the FPA is cooled from room temperature to the operating temperature. Despite early concern over the stability of the bump interconnections, the devices have exhibited > 99 per cent interconnection yield and excellent reliability. Figure 3 illustrates the direct backside illuminated configuration, which is favoured for $N \times N$ staring FPAs. The largest reported to date direct 2-D array is SW 2048 \times 2048 FPA with $18 \mu\text{m} \times 18 \mu\text{m}$ unit cell areas¹¹. In the indirect backside illuminated configuration, both the $HgCdTe$ detector array and the silicon ROIC chip are bump-mounted side-by-side onto a common circuit board. The indirect configuration allows the unit cell area in the silicon ROIC chip to be larger

than the detector area and is usually used for small scanning FPAs, where stray capacitance is not an issue.

In the frontside illuminated configuration, electrical interconnect between each detector and its corresponding input circuit is made through a small hole formed in each detector. The junctions are connected down to the silicon circuit by cutting the fine (few micron in diameter) holes through the junctions by ion milling, and then backfilling the holes through metallisation. The thermal expansion mismatch problem is approached by using about $10 \mu\text{m}$ thick p -type $HgCdTe$, bonded rigidly to the silicon so that strain is taken up elastically. This makes the devices mechanically and electrically very robust with contact obscuration typically < 10 per cent. The disadvantages include the necessity of mechanical thinning of the $HgCdTe$, which may

Table 1. *HgCdTe* photodiode architectures used for hybrid FPAs¹²

Configuration	Junction formation	Company
<i>n-on-p</i> VIP	Ion implantation forms <i>n-on-p</i> diode in <i>p</i> -type <i>HgCdTe</i> , grown by <i>Te</i> -solution LPE on <i>CdZnTe</i> and epoxied to silicon ROIC wafer; over the edge contact	DRS Infrared Technologies (formerly Texas Instruments)
<i>n-p</i> loophole	Ion beam milling forms <i>n</i> -type islands in <i>p</i> -type <i>Hg</i> -vacancy-doped layer grown by <i>Te</i> -solution LPE on <i>CdZnTe</i> , and epoxied onto silicon ROIC wafer; cylindrical lateral collection diodes	GEC-Marconi Infrared (GMIRL)
<i>n</i> ⁺ - <i>on-p</i> planar	Ion implant into acceptor-doped <i>p</i> -type LPE film grown by <i>Te</i> -solution slider	Sofradir (<i>Societe Francaise de Detecteurs Infrarouge</i>)
<i>n</i> ⁺ - <i>n</i> ⁻ planar homojunctions	Boron implant into <i>Hg</i> -vacancy <i>p</i> -type, grown by <i>Hg</i> -solution tipper on 3 in. diameter sapphire with MOCVD <i>CdTe</i> buffer; <i>ZnS</i> passivation	Rockwell/Boeing
<i>P-on-n</i> mesa	1. Two-layer LPE on <i>CdZnTe</i> : Base: <i>Te</i> -solution slider, indium-doped Cap: <i>Hg</i> -solution dipper, arsenic-doped 2. MOCVD <i>in situ</i> on <i>CdZnTe</i> Iodine-doped base, arsenic-doped cap	IR Imaging Systems, Sanders – A Lockheed Martin Co. (LMIRIS)
<i>P-on-n</i> mesa	1. Two-layer LPE on <i>CdZnTe</i> : Base: <i>Te</i> -solution slider, indium-doped Cap: <i>Hg</i> -solution dipper, arsenic-doped 2. MOCVD <i>in situ</i> on <i>CdZnTe</i> Iodine-doped base, arsenic-doped cap	Raytheon Infrared Centre of Excellence (RIRCoE, formerly SBRC) and Hughes Research Laboratories (HRLs)
<i>P-on-n</i> planar buried heterostructure	Arsenic implant into indium-doped <i>N-n</i> or <i>N-n-N</i> film grown by MBE on <i>CdZnTe</i>	Rockwell/Boeing

lead to damage that may affect photodiode performance and the necessity of devising clever low temperature techniques for junction formation and passivation because of the presence of the epoxy (e.g. the ion milling process to form the *n*-type regions is done at room temperature).

Different *HgCdTe* photodiode architectures have been fabricated compatible with backside and frontside illuminated hybrid FPA technology. Cross-section views of these architectures are shown in Figs 4 and 5. The important architectures are also included in Table 1, which summarises the applications of *HgCdTe* photodiode designs by the major FPA manufacturers.

Table 2 contains description of representative *HgCdTe* FPAs, commercially available and described on websites of the major *HgCdTe* manufactures. The LWIR FPAs are usually operated at 77K and are near the BLIP limit for higher background fluxes. The MWIR FPAs that

operate above 77K, often are thermoelectrically cooled. Their operation temperature depends on the design of the ROIC chip. Standard products for SWIR may be operated at room temperature. Table 2 does not contain a complete list of products, but it illustrates the range of *HgCdTe* FPAs wavelengths, formats, unit cell size, and the FPA performance [detectivity (D^*), and noise equivalent different temperature (NEDT)], that can be considered to be commercially available.

3.2 Frontside Illuminated Photodiodes

The frontside illuminated *n-on-p* homojunction was the first *HgCdTe* device structure pioneered by the *Societe Anonyme de Telecommunications*¹³ (SAT). Mercury in-diffusion into vacancy-doped *HgCdTe* has been a widely used technique for very fast photodiodes¹⁴. Mercury is diffused through openings formed in an insulator layer, lowering the mercury vacancy concentration below that of the donors, which are either intentionally introduced

Table 2. Representative *HgCdTe* FPAs offered by some of the major manufacturers

Cut-off wavelength (μm)	FPA size	Unit cell (μm^2)	D^* ($\text{cmHz}^{1/2} \text{W}^{-1}$) NEDT (mK)	Manufacturer
LW	240/288 \times 4 TDI	44 \times 51	2.8×10^{11}	Raytheon IR Centre of Excellence (RIRCoE, formerly SBRC) (www.sbrc.com)
11.00	64 \times 64	61 \times 61	≈ 30	
11.00	128 \times 128	40 \times 40		
11.00	256 \times 256	30 \times 30		
MW	432 \times 432			IR Imaging Systems, Sanders – A Lockheed Martin Co. (LMIRIS) (www.sanders.com/iris)
MW	768 \times 768			
LW	64 \times 64	60 \times 60		
LW	256 \times 256	30 \times 30		
2.50	2048 \times 2048	18.5 \times 18.5	1×10^{14}	Rockwell/Boeing (www.rsc.rockwell.com/mct_fpa/)
5.00	1024 \times 1024	18.5 \times 18.5	$> 4 \times 10^{11}/<25$	
4.85	320 \times 240	30 \times 30	$> 4 \times 10^{11}$	
4.85	256 \times 256	40 \times 40	$> 4 \times 10^{11}$	
>10.00	640 \times 480	27 \times 27		
>15.00	256 \times 256	40 \times 40		
4.80	480 \times 6 TDI	38 \times 28	6.9×10^{11}	<i>Sofradir (Societe Francaise de Detecteurs Infraouge)</i> (www.sofradir.com)
10.30	480 \times 6 TDI	38 \times 28	3.5×10^{11}	
4.80	128 \times 128	50 \times 50	$4.4 \times 10^{11}/7$	
10.00	128 \times 128	50 \times 50	$1.1 \times 10^{11}/10$	
4.80	320 \times 240	30 \times 30	$5.6 \times 10^{11}/8$	
9.50	320 \times 240	30 \times 30	$1.7 \times 10^{11}/18$	
5.00	384 \times 288	20 \times 20	15	
10.00	576 \times 6 TDI	30 \times 30	25	
10.00	768 \times 8 TDI	30 \times 30	20	GEC-Marconi Infrared (GMIRL) (www.gec-marconi.com)
5, 10.00	256 \times 256	40 \times 40	15, 20	AIM (AEG Infrared-Modules GmbH) Phone: 49-7131-6212-24 Fax: 49-7131-1782-91
5.00	384 \times 288	24 \times 24	25	
5.00	640 \times 512	24 \times 24	< 20	
10.50	128 \times 1	20 \times 40	8×10^{10}	SCD (Semi-Conductor Devices) (www.scd.co.il)
10.50	256 \times 1	24 \times 24	8×10^{10}	
10.50	480 \times 6	35 \times 28		

dopants or residual impurities. For this device structure, the first time use of an interdiffused *CdTe* layer for heterostructure passivation was reported¹⁵.

Conversion of vacancy-doped *p*-type *HgCdTe* to *n*-type during low energy ion milling became another important technique of junction fabrication [Fig. 3(b)]. GEC-Marconi Infrared Laboratories uses 25 μm –30 μm LPE layer (grown from tellurium-rich solution) epoxied to a silicon CMOS ROIC¹⁶ chip. Small holes, (5 μm in diameter), are created by ion milling. Just as in the case of ion-implanted *n*-on-*p* junction, the *n*-type region is formed when mercury atoms are liberated during the milling process. Mercury atoms diffuse

laterally, annihilating mercury vacancy acceptors and uncovering residual and intentional donors. The detector processing incorporates a metallisation of small holes which connects one side of the junction to the input circuit node directly beneath. In this device geometry, photocarriers are collected by lateral diffusion, and R_0A products are generally lower than are achieved in junctions with extrinsically doped absorber layer, due to short lifetime in the vacancy-doped *p*-type material.

Technology of the frontside-illuminated *n*-on-*p* vertically integrated photodiode (VIP) used by data retrieval systems (DRSS)¹⁷ is similar to the lateral loophole technology. The VIP process

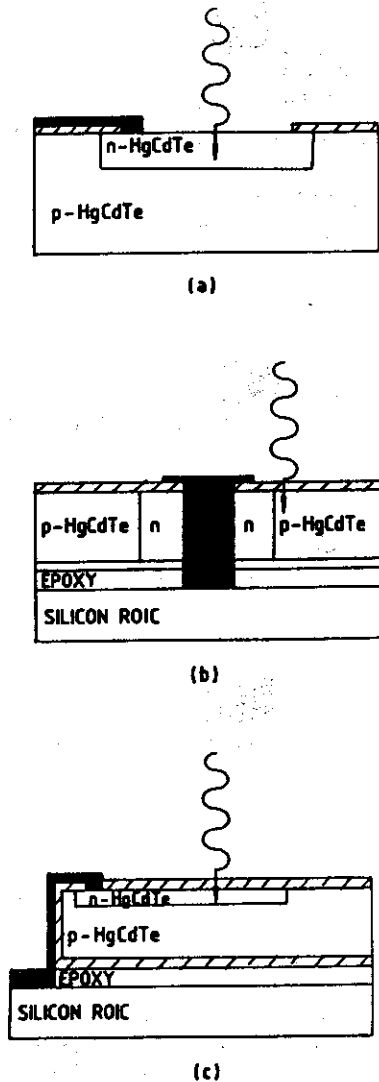


Figure 4. Frontside illuminated *HgCdTe* photodiode architectures: (a) Planar *Hg*-diffused *n-on-p* homojunction, (b) *n-p* loophole homojunction, and (c) *n-on-p* vertically integrated photodiode.

employs a planar, ion-implanted *n-on-p* junction in *HgCdTe* which is epoxied to a silicon CMOS ROIC. A *via* hole is etched, and an over-the-edge contact metallisation connects each junction area with an input node in the silicon ROIC below.

3.3 Backside Illuminated Photodiodes

The first architecture used for hybrid *HgCdTe* FPAs was backside illuminated planar ion-implanted n^+n^-p homojunction [Fig. 5(a)]. The base *p*-type absorber layer was grown by LPE onto an IR transparent substrate, such as *CdTe*, *CdZnTe*

or sapphire. During implantation, interstitial mercury atoms are liberated, diffused inward, annihilating mercury vacancies and forming an *n*-region beneath the n^+ -implanted layer¹⁸. In non-doped *HgCdTe*, the acceptors are the mercury vacancies and short lifetime in *p*-type region and suppressed R_0A values are observed. Factors of ten higher R_0A values ($655 \Omega\text{cm}^2$ at 77K, $\lambda_c = 10 \mu\text{m}$) for this structure were attributed to higher lifetime in the acceptor-doped *p*-type absorber layer, but there was no explanation for how longer lifetime was achieved¹⁹. The theoretically predicted Auger-limited value of R_0A , equal to $680 \Omega\text{cm}^2$, is nearly identical to the experimental value²⁰.

To reduce the detector cooling requirements, British workers proposed nonequilibrium photodiode structures which employ both minority carrier exclusion and minority carrier extraction to suppress the Auger generation^{21,22}. This type of device, the *P- π -N* structure (the capital letter denotes a region of wider band gap) is shown in Fig. 5(b). The low-doped *p*-type absorber layer is sandwiched between wider-gap *n*-type and *p*-type layers. The π -type layer is electrically neutral; only a narrow depletion region occurs at the π -*N* interface. This junction is operated in reverse bias producing extraction of minority carriers. The other, isotype junction is excluding to minority carriers preventing their injection into the π layer. Under these conditions, the electron concentration is negligible and hole concentration is lowered to the extrinsic acceptor concentration. The thermal generation rates due to the Auger 1 and Auger 7 mechanisms are reduced substantially. The non-equilibrium devices have been realised in different configurations, and more recently in sophisticated five-layer films grown *in situ* by MOCVD with cut-off wavelengths ranging between $7.5 \mu\text{m}$ and $10.5 \mu\text{m}$ at room temperature⁹. However, the Auger suppression devices suffer from large $1/f$ noise and hence the improvement in the detectivity resulting from the reduced leakage currents can only be realised at high frequencies.

Next four device structures shown in Figs 5(c), 5(d), 5(e) and 5(f), are based on *P-on-n*

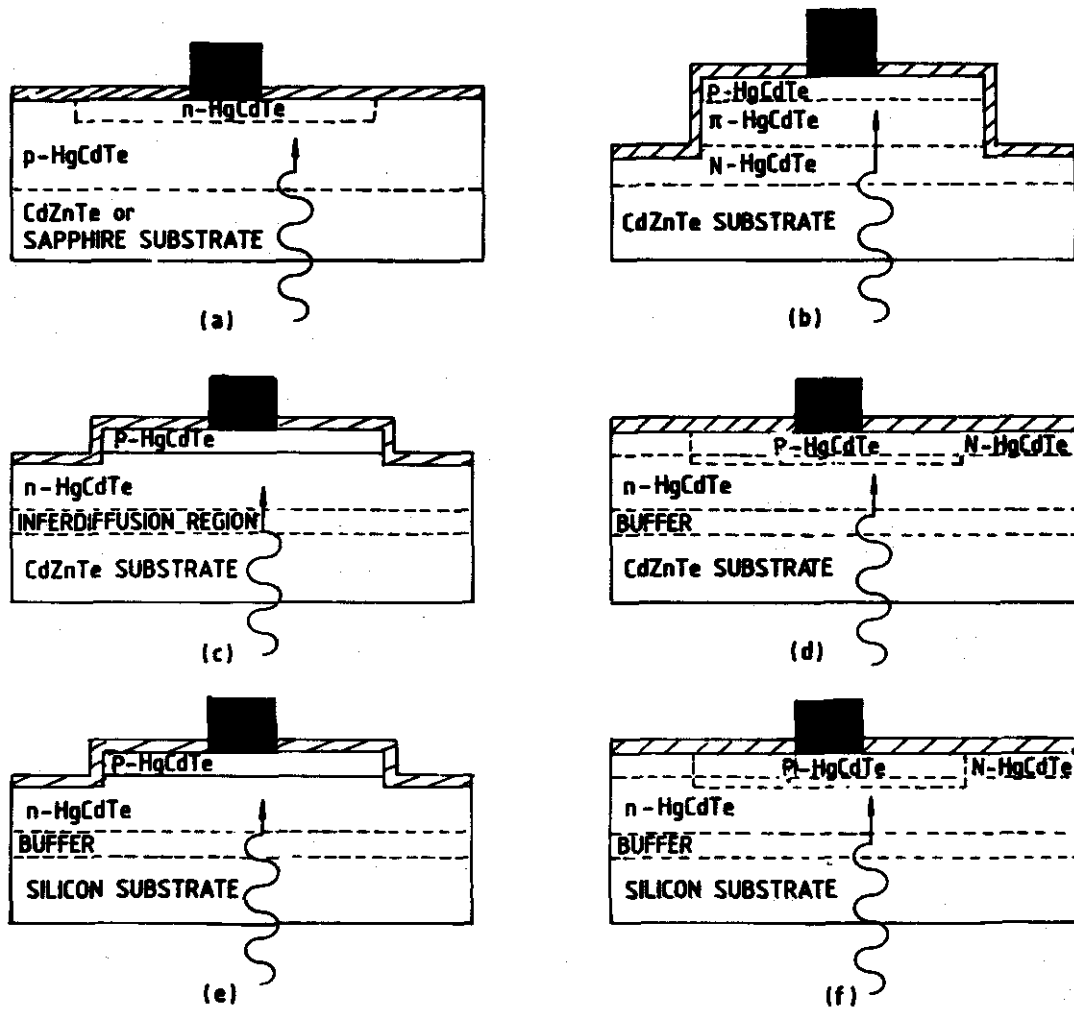


Figure 5. Backside illuminated $HgCdTe$ photodiode architectures: (a) Planar ion-implanted n^+-n-p homojunction, (b) $P-\pi-N$ nonequilibrium photodiode, (c) backside illuminated mesa P -on- n heterojunction, (d) backside illuminated arsenic-implanted $P-n-N$ planar buried junction heterostructure, (e) backside illuminated mesa P -on- n heterojunction on silicon substrate, and (f) backside illuminated arsenic-implanted $P-n-N$ planar buried junction heterostructure on silicon substrate.

heterostructures. The backside illuminated mesa P -on- n heterojunction [Fig. 5(d)] has become the widely used junction architecture for bump-mounted hybrid FPAs. In this so called double-layer heterojunction (DLHJ) structure, about $10\ \mu\text{m}$ absorber layer is doped with indium at $1 \times 10^{15}\ \text{cm}^{-3}$ or less, and is grown either by horizontal-slider LPE from tellurium-rich solution or by vertical-dipper LPE from mercury-rich solution. The p -type cap layer with wider band gap energy ($\Delta x \approx 0.04$) is doped with arsenic around $(1-4) \times 10^{17}\ \text{cm}^{-3}$ and is grown by vertical-dipper LPE from mercury-rich solution. Several factors favoured the n -type absorber over the p -type

absorber. The n -type $HgCdTe$ at low carrier concentrations is easier to control and passivate, and is comparatively free of the Shockley-Read defects that limited the lifetime of p -type material.

The small gradients in $HgCdTe$ absorber layer cause small gradients in energy band gap, which, for backside illuminated LPE photodiodes, have the beneficial effect of setting up an effective electric field that provides drift-associated collection of photogenerated carriers. Also, a thin ($2\ \mu\text{m}-4\ \mu\text{m}$) interdiffused layer between the n -type absorber and the substrate causes an effect that carriers are repelled away from the interface, thereby preventing recombination at the defects present

at this interface. The critical parameters – composition difference across the heterojunction (Δx), composition gradient, placement of the P - n junction relative to the composition junction, and base dopant concentration (N_d) – are technology-specific to each material growth process and are discussed in detail by Reine¹². Barriers are more troublesome for very long-wavelength infrared (VLWIR) photodiodes because the rate of compositional interdiffusion increases with decreasing x -value²³.

The unique feature of the structure shown in Fig. 5(d), the backside illuminated arsenic-implanted P - n - N planar-buried heterostructure, is that the junction is buried beneath the top wide-band gap n -type layer. The junction intersects the surface in wider-band gap $HgCdTe$, thereby reducing the generation rates for any surface defect and prevents carrier recombination at this interface. The arsenic-doped p -type region must extend sufficiently deep into narrow-band gap absorber layer to effectively collect photocarriers. The P - n - N device structures are fabricated using low temperature *in situ* growth and band gap engineering provided by MBE onto a $CdZnTe$ substrate, while the junctions are formed by arsenic implantation. To activate arsenic an acceptor, it must occupy a tellurium site in the lattice. Full arsenic activation is achieved for annealing at 300 °C or higher. As per Arias²⁴, *et al.*, the sample underwent two consecutive annealings, one at about 430 °C (to diffuse the arsenic into the base layer) for approximately 10 min and the other at 250 °C (to annihilate mercury vacancies formed in the $HgCdTe$ lattice during growth and diffusion of arsenic). The electrical junction is positioned near the metallurgical interface and it is wise to place the junction in the small band gap layer to avoid deleterious effects on the quantum efficiency and dark currents. At present, the researchers are using $CdTe$ or $CdZnTe$ (deposited by MBE, MOCVD, sputtering and e-beam evaporation) for photodiode passivation²⁵.

Near lattice-matched $CdZnTe$ substrates have severe drawbacks, such as lack of large area, high production cost, and more important, the difference of thermal expansion coefficient in $CdZnTe$

substrates and silicon ROICs as well as interest in large area-based IR FPAs (1024 × 1024 and larger), have resulted in $CdZnTe$ substrate application limitations. The use of silicon substrates is very attractive in IR FPA technology not only because it is less expensive and available in large area wafers but also because in an FPA structure, the coupling of the silicon substrates with silicon ROICs allows the fabrication of very large arrays exhibiting long-term thermal cycle reliability.

Despite the large lattice mismatch (≈ 19 per cent) between $CdTe$ and silicon, MBE has been successfully used for the heteroepitaxial growth of $CdTe$ on silicon. Since 1989, Santa Barbara Research Centre has successfully utilised infinite-melt vertical LPE technology from mercury-rich solution to grow high quality epitaxial $HgCdTe$ on the silicon-based alternative substrates for the fabrication of p -on- n DLHJ detectors for high performance²⁶ MWIR FPAs. During the past several years, progress has been made in the growth of MBE and MOCVD $CdTe$ on silicon substrates as well as MBE and MOCVD- $HgCdTe$ growth on these alternative substrates. Different procedures have been used to fabricate composite substrates. de Lyon²⁷, *et al.* have fabricated buffer layer structures consisting of 1 μm layer of $ZnTe$, followed by 8 μm , $CdTe$ grown at 1.0 $\mu\text{m/hr}$ at silicon(112) substrate at 270 °C. A more complex procedure has been used by Wijewarnasuriya²⁸, *et al.* Following special chemical treatment and predeposition of few $SiTe_2$ monolayers (created by exposing the surface to Te flux), a thin $ZnTe$ layer was grown at 220 °C followed by 10 min annealing under $CdTe$ and Te flux at 380 °C. Finally, $CdTe(211)B$ layer was grown at 300 °C. Using optimised growth condition for silicon (211)B substrates, $CdTe(211)B$ layers with etch-pit-density (EPD) of 10^5 cm^{-2} to 10^6 cm^{-2} range could be obtained.

The last two $HgCdTe$ photodiode architectures shown in Figs 5(e) and 5(f) can be fabricated using silicon substrates.

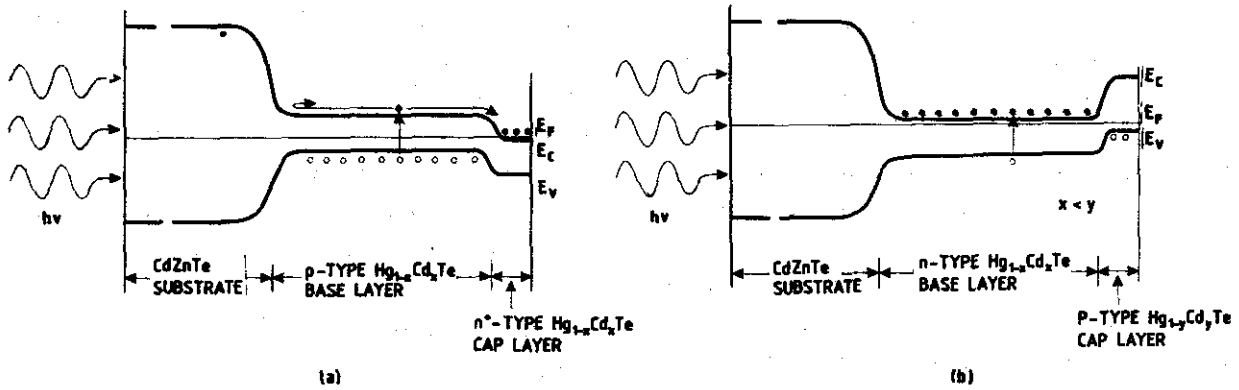


Figure 6. Schematic band diagrams of n^+ -on- p homojunction: (a) P -on- n heterojunction photodiodes.

4. FUNDAMENTAL LIMITATION TO $HgCdTe$ PHOTODIODE PERFORMANCE

One can distinguish two fundamental $HgCdTe$ photodiode architectures based on p -type absorber layer (simple n^+ -on- p homojunction) and n -type absorber layer (P -on- n heterojunction) considering results obtained. Necessity of using heterojunction n -type absorber layer is theoretically evidenced²⁰. Figure 6 shows the schematic band profiles of the unbiased homo- and heterojunction photodiodes. To avoid contribution of the tunnelling current, the doping concentration in the base region below 10^{16} cm^{-3} is required. In both photodiodes, the lightly doped narrow gap absorbing region [base of the photodiode: $p(n)$ -type carrier concentration of about $5 \times 10^{15} \text{ cm}^{-3}$ ($5 \times 10^{14} \text{ cm}^{-3}$)], determines the dark current and photocurrent. The base p -type layers (or n -type layers) are sandwiched between $CdZnTe$ substrate and high doped (in n^+ -on- p structures) or wider gap (in P -on- n structure) regions. Due to backside illumination (through $CdZnTe$ substrate) and internal electric fields (which are blocking for minority carriers), influence of surface recombinations on the photodiodes performance is eliminated. The influence of surface recombination can also be prevented using suitable passivation. Both optical and thermal generations are suppressed in the n region due to the Burstein-Moss effect and in the P -region due to wide gap. Since the base region determines largely the properties of the device, it should be carefully optimised.

The thickness of the base region should be optimised for near unity quantum efficiency and a low dark current. This is achieved with a base thickness slightly higher than the inverse absorption coefficient for single pass devices: $t = 1/\alpha$ (which is $\approx 10 \mu\text{m}$) or half of the $1/\alpha$ for double pass devices (devices supplied with a retroreflector). Low doping is beneficial for low thermal generation and high quantum efficiency. Since the diffusion length in absorbing region is typically longer than its thickness, any carrier generated in the base region can be collected giving rise to the photocurrent.

Assuming that the Auger mechanisms impose fundamental limitations to the $HgCdTe$ photodiode performance and that the saturation dark current, I_s , is only due to thermal generation in the base layer and that its thickness, t , is low compared to the diffusion length:

$$I_s = GtqA \quad (2)$$

where G is the generation rate in the base layer, q is standard Coulomb charge and A is the detector area. Then R_0A is:

$$R_0A = \frac{kT}{q^2 Gt} \quad (3)$$

Taking into account the Auger 7 mechanism in extrinsic p -type region of n^+ -on- p photodiode, one receives:

$$R_0A = \frac{2kT\tau_{A7}'}{q^2N_a t} \quad (4)$$

and the same equation for *P*-on-*n* photodiode is:

$$R_0A = \frac{2kT\tau_{A1}'}{q^2N_d t} \quad (5)$$

where N_a and N_d are the acceptor and donor concentrations in the base regions, respectively.

As Eqns (4) and (5) show, the R_0A product can be decreased by reducing the thickness of the base layer. Since $\gamma = \tau_{A7}' / \tau_{A1}' > 1$, a higher R_0A value can be achieved in *p*-type base devices compared to that of *n*-type devices of the same doping level. Detailed analysis shows that the absolute maximum of R_0A is achievable with base layer doping producing $p = \gamma^{1/2}n_i$, which corresponds to the minimum of thermal generation. The required *p*-type doping is difficult to achieve in practice for low temperature photodiodes (the control of hole concentration below $5 \times 10^{15} \text{ cm}^{-3}$ level is difficult) and the *p*-type material suffer from some non-fundamental limitations, such as contacts, and surface and Shockley-Read processes. These are the reasons why the low temperature detectors are typically produced from the lightly doped *n*-type materials.

4.1 Long-Wavelength Infrared Photodiodes

The dependence of the base region diffusion-limited R_0A product on the long wavelength cut-off for n^+p *HgCdTe* photodiodes at $\leq 77\text{K}$ is shown in Fig. 7. At 77K the experimental results show a greater spread, probably due to additional currents in the junctions. *P*-type base material is characterised by relatively high trap concentration, which dominates the excess carrier lifetime by the Shockley-Read-Hall recombination mechanism. Its influence depends on technological limits. At operating temperatures $< 77\text{K}$, two other distinct mechanisms dominate the dark current: trap-assisted tunnelling and band-to-band tunnelling. Multi-step recombination *via* defects plus variations in local-electrical parameters were

probably the reasons that the expected strong band-to-band gap effect on devices was not observed as evidenced in the 77K data for the best photodiodes, where the currents are diffusion-limited. However, the quality of *p*-type material has been considerably improved by acceptor doping¹⁹. R_0A improvement of one order of magnitude (in the range between $400 \text{ } \Omega\text{cm}^2$ to $650 \text{ } \Omega\text{cm}^2$ at 77K for a $10 \text{ } \mu\text{m}$ cut-off wavelength detector) has been observed. This effect was obtained as a result of an increase in the minority carrier lifetime in the base *p*-type region (close to the Auger 7-limited lifetime) and a slightly thinner epitaxial *p*-type layer. The experimental data agree approximately with theoretical predictions¹⁹⁻²⁰ for the temperature range between 77K to 50K.

The dependence of the base region diffusion-limited R_0A product on the long wavelength cut-off for *P*-on-*n* LWIR *HgCdTe* photodiodes at different temperatures is shown in Fig. 8. This figure also includes the experimental data for DLHJ *P*-on-*n* structures. The wider band gap cap layer contributes a negligible amount of thermally generated diffusion current compared to that from an *n*-type absorber layer at 77K, and the upper experimental data are situated about a half-of-an-order below ultimate theoretical predictions. With a lowering of the operation temperature of photodiodes, the discrepancy between the theoretical curves and the experimental data increases, which is due to additional currents in the junctions (such as tunnelling current or surface leakage current) that are not considered. Photodiodes with lower performance usually contain metallurgical defects, such as dislocation clusters and loops, pinholes, striations, tellurium inclusions, and heavy terracing. It should be noticed that the upper experimental data in long wavelength range (above $14 \text{ } \mu\text{m}$) at lower temperature (40K) coincides very well with theoretical predictions. The best devices continued to be diffusion-current limited by Auger mechanism at zero bias to 35 K. At 40K, the measured R_0A is $2 \times 10^4 \text{ } \Omega\text{cm}^2$ and the measured cut-off wavelength is $17.6 \text{ } \mu\text{m}$. At 35K, R_0A is $2 \times 10^5 \text{ } \Omega\text{cm}^2$ at cut-off wavelength $18.1 \text{ } \mu\text{m}$.

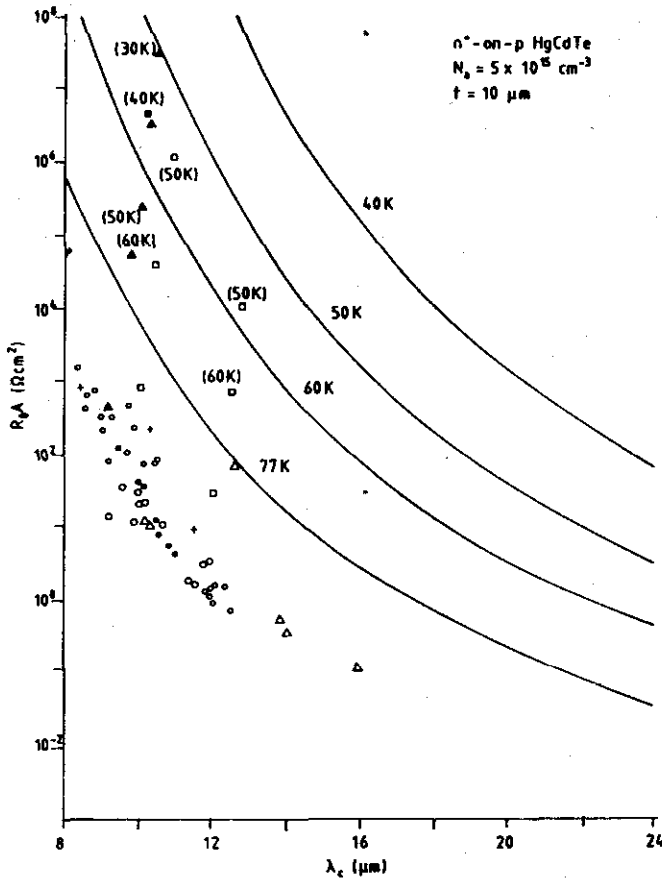


Figure 7. Dependence of R_0A product on the long-wavelength cut-off for LWIR n^+ -on- p $HgCdTe$ photodiodes at temperatures $\leq 77K$. The solid lines are calculated assuming that the performance of photodiodes are due to thermal generation governed by the Auger mechanism in the base p -type region of photodiodes with $t = 10 \mu m$ and $N_d = 5 \times 10^{15} cm^{-3}$.

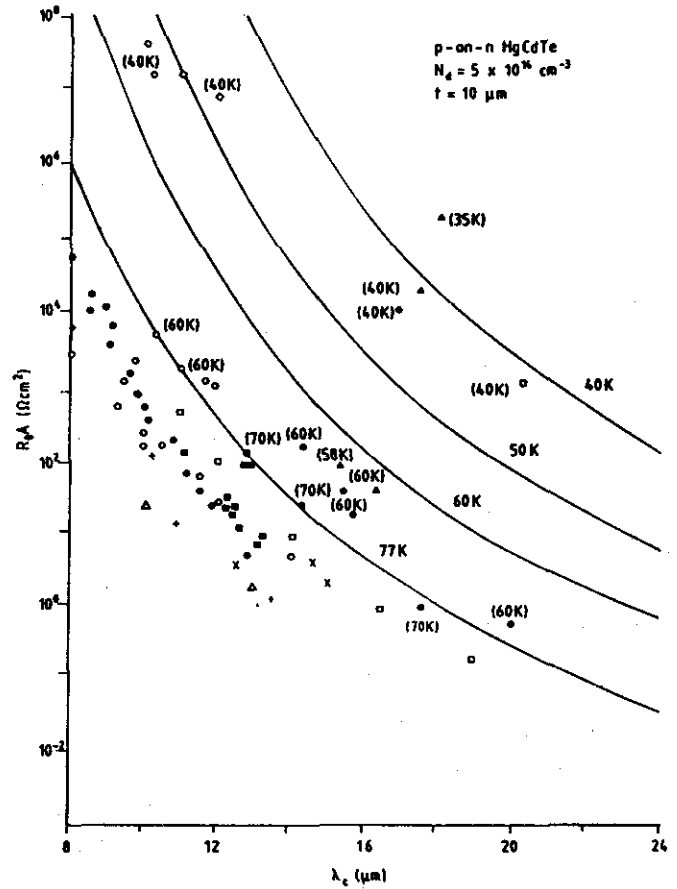


Figure 8. Dependence of R_0A product on the long-wavelength cut-off for LWIR P -on- n $HgCdTe$ photodiodes at temperatures $\leq 77K$. The solid lines are calculated assuming that the performance of photodiodes are due to thermal generation governed by the Auger mechanism in the base n -type region of photodiodes with $t = 10 \mu m$ and $N_d = 5 \times 10^{14} cm^{-3}$.

Also the performance of photodiodes with cut-off wavelengths of $20.3 \mu m$ at $40K$ is diffusion-limited and R_0A products for the diodes reach values in the $10^3 \Omega cm^2$ range. These are the highest reported values at these long cut-off wavelengths for any $HgCdTe$ device.

Comparing Figs 7 and 8, one can see that for assumed doping concentrations in the base region of photodiodes ($N_d = 5 \times 10^{15} cm^{-3}$ for n^+ - p structure and $N_d = 5 \times 10^{14} cm^{-3}$ for P - n structure) and for a given cut-off wavelength, the theoretical values of R_0A product for P -on- n photodiodes range $< 77K$ are a little greater than for n -on- p photodiodes. However, $200K$ – $300K$ LWIR devices exhibit the same R_0A values since the base layer materials

becomes intrinsic in both cases. It should be noted that more heavy p -type doping is necessary for the best photodiode performance at high temperature operation³⁰.

Figure 9 compares the results of LWIR arrays fabricated on MBE-grown $CdZnTe/Si$ and MOCVD-grown $CdZnTe/GaAs/Si$ with historical trendlines of arrays fabricated on bulk $CdZnTe$ ³¹. Each data point represents the array average R_0A product measured at $f/2$ FOV (300 K) background at 78 K. LWIR $Hg_{0.77}Cd_{0.23}Te$ DLHJ was grown by vertical-LPE from infinite melt mercury-rich solutions. The n -type base layer was doped with indium and the wider-band gap layer was doped with arsenic. The two continuous curves shown in

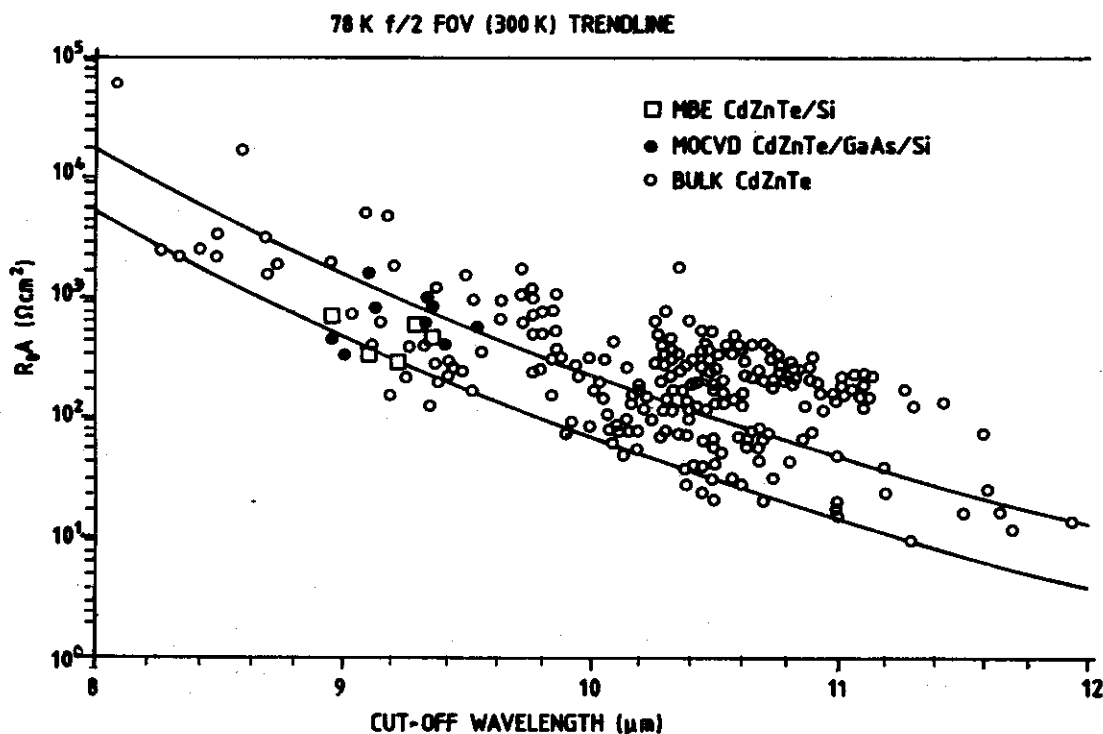


Figure 9. Comparison of the results of LWIR $HgCdTe$ arrays fabricated on MBE-grown $CdZnTe/Si$ and MOCVD-grown $CdZnTe/GaAs/Si$ with historical trendlines of arrays fabricated on bulk $CdZnTe$. Each data point represents the array average R_0A product measured at $f/2$ FOV (300K) background at 78K.

Fig. 9 were calculated to indicate diffusion-limited behaviour and were only shown as a guide to the eye. We can see that there is no significant difference between arrays fabricated on either $CdZnTe/Si$ or $CdZnTe/GaAs/Si$, and the results on these silicon-substrates are comparable with results on bulk $CdZnTe$ substrates at 78K. To improve reverse-bias characteristics at 78K and detector performance at lower temperatures in comparison with bulk $CdZnTe$ substrates, a further reduction in the dislocation density for $HgCdTe$ grown on silicon-based substrates is needed.

4.2 Mid-Wavelength Infrared Photodiodes

MWIR $HgCdTe$ photodiodes were the first to be developed, and many mature technologies have been used to demonstrate FPAs^{32,33}. Rockwell hence has developed the capability for fabricating large MWIR $HgCdTe$ FPAs by epitaxially growing $HgCdTe$ on sapphire (PACE-1 process). In this process, a $CdTe$ layer is grown *via* MOCVD on the sapphire and next $HgCdTe$ is grown on the $CdTe$ buffer *via* LPE. The junctions are formed by boron

ion implantation and thermal annealing. Planar and mesa junctions are used, depending on the FPA specifications, and are passivated with a ZnS or $CdTe$ film. The detector array is backside illuminated through the sapphire substrate, which transmits to $6.5 \mu m$ for a 7 mil thickness. PACE-1 process currently provides intrinsic detector arrays with BLIP performance and satisfactory yield.

Sapphire substrate offers several attributes. Its thermal coefficient of expansion matches well with the alumina chip carrier, thereby greatly improving large hybrid reliability. The large substrate also reduces detector cost by increasing throughput, enabling batch processing and reducing breakage. The 7.62 cm (3 in.) wafers, currently in production, enable populating each wafer with either five $18.5 \mu m$ pixel 1024×1024 arrays (in addition to four $40 \mu m$ 256×256 arrays), eight $27 \mu m$ 640×480 arrays, or twenty-one 256×256 arrays.

Since 1989, SBRC has successfully utilised infinite-melt vertical LPE technology from Hg -rich solution to grow high quality epitaxial $HgCdTe$ on

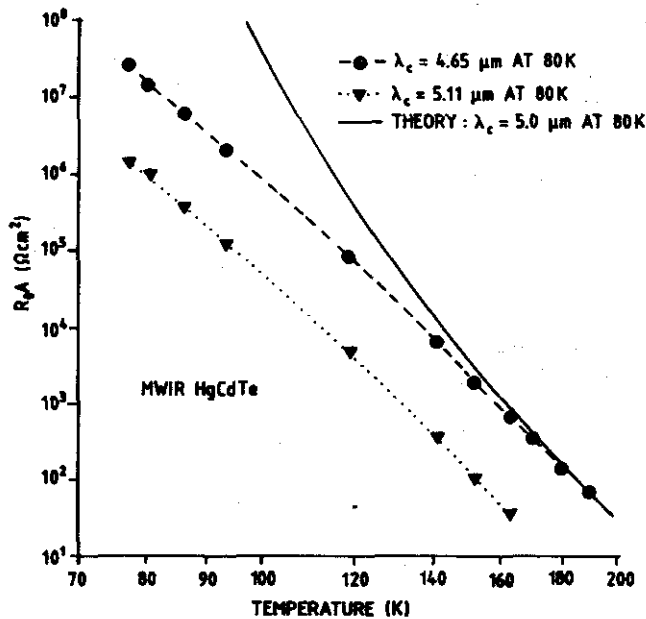


Figure 10. R_0A product versus temperature for MWIR $HgCdTe$ photodiodes.

the silicon-based alternative substrates for the fabrication of p -on- n DLHJ detectors for high performance MWIR FPAs. Tung²⁶, *et al.* reported large, up to 480×640 , MWIR FPAs, grown on silicon-based alternative substrates.

Figure 10 compares R_0A product for two PACE MWIR $HgCdTe$ layers with cut-off wavelengths at 78K of $5.11 \mu m$ and $4.65 \mu m$, respectively versus temperature. Also compared is the theoretical R_0A performance for $5 \mu m$ p -on- n $HgCdTe$ photodiode; this level is readily achieved with MBE MWIR DLHJ $HgCdTe/CdZnTe$ material³⁴. A buried planar heterostructure produces devices whose performance is less critical of passivation as compared to conventional mesa technology because the junction interface is buried. The planar p -on- n photodiodes are formed by selective pocket diffusion of arsenic (a p -type dopant), which is deposited by ion implantation on the wide band gap cap layer.

MBE-grown devices on silicon and $CdZnTe$ appear to be identical³⁵. Figure 11 presents a comprehensive comparison of the performance of MWIR P -on- n $HgCdTe$ photodiodes on $CdZnTe$ and

silicon substrates for cut-off wavelengths ranging from $3.5 \mu m$ to $5.0 \mu m$. The various data points are median values for mini arrays included in test structures for each processed wafer. The devices with highest performance are processed from MBE-grown epilayers on bulk $CdZnTe$ substrates. The shorter cut-off devices (with $\lambda_c \approx 3 \mu m$) are diffusion-limited down to at least 125K. The devices with longer cut-off wavelength (with $\lambda_c \approx 5 \mu m$) appear to be diffusion-limited down to approximately 110K. Below this temperature, the experimental data obscure the probable onset of generation-recombination and/or tunnelling current limitations.

4.3 Short-Wavelength Infrared Photodiodes

Considerable progress in $HgCdTe$ SWIR hybrid FPAs has been achieved in the last decade. At the beginning, the detector arrays were fabricated using a n^+ boron-implanted process on p -type $HgCdTe$ layers grown by LPE on $CdTe$ or $CdZnTe$ substrates³². Next, the PACE-1 process was adopted to fabricate large, $2.5 \mu m$ 1024×1024 FPAs (HAWAII) for IR astronomy^{36,37}. Recently,

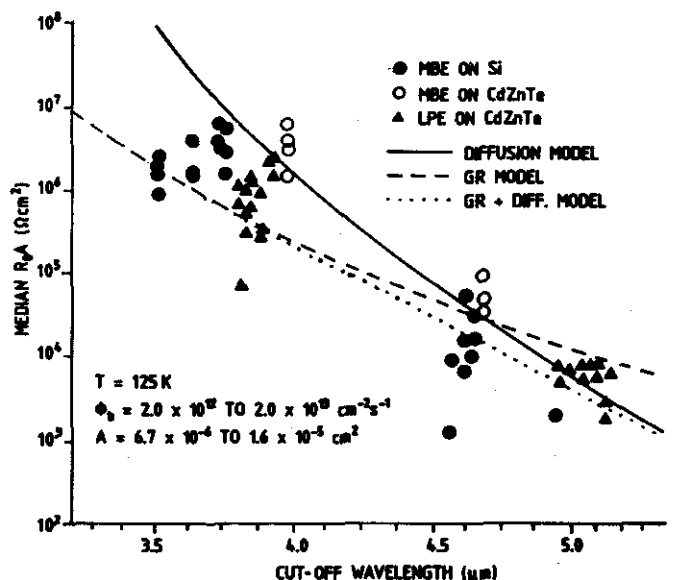


Figure 11. Comparison of 125K detector performance for MWIR $HgCdTe$ photodiodes grown on silicon and $CdZnTe$ by MBE and photodiodes grown on $CdZnTe$ by LPE. Each data point represents an array-median R_0A product measured at 125K.

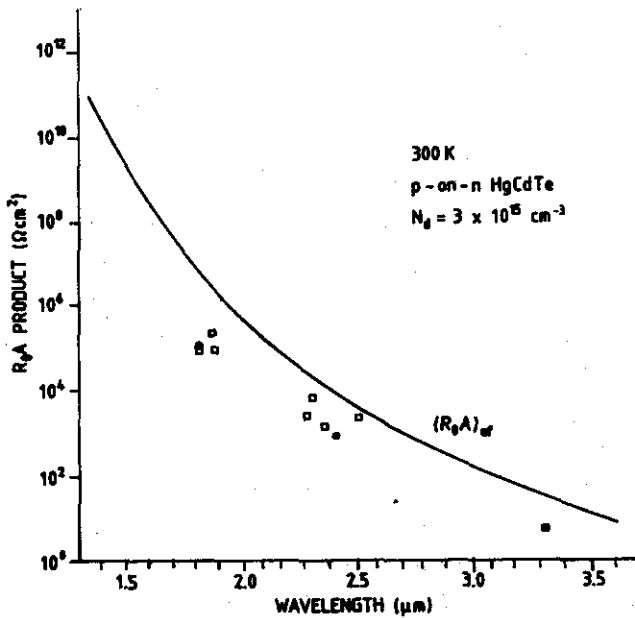


Figure 12. Dependence of effective R_0A product on the long-wavelength cut-off for SWIR $HgCdTe$ photodiodes at room temperature. The calculations are performed assuming that the performance of photodiodes is due to fundamental generation-recombination processes in the base p -type region of photodiodes with $t = 5 \mu m$ and $N_a = 3 \times 10^{15} cm^{-3}$.

double-layer planar heterostructure (DLPH) p -on- n photodiodes in MBE $HgCdTe$ on $CdZnTe$ substrates have been elaborated by arsenic-ion implantation and the p -dopant activation by an open-tube mercury anneal³⁸.

The highest detector performance is achieved by growing the layers on lattice-matched substrates, such as $CdZnTe$ (their properties are least affected by threading dislocations). Adding indium during growth provided donor doping nominally $1.5 \times 10^{15} cm^{-3}$ with a majority carrier mobility of $\approx 8000 cm^2/Vs$ at 77K. MBE DLHJ $HgCdTe/CdZnTe$ photodiodes are made using a buried planar heterostructure. Typical active layer thickness is $\approx 3.5 \mu m$ and cap layer thickness³⁸ is $\approx 0.4 \mu m$. The highest quality SWIR $HgCdTe$ photodiodes have performance in agreement with the radiative limit. It appears, however, that due to photon recycling, an order of magnitude enhancements in the radiative lifetimes over those obtained from the standard van Roosbroeck and Shockley expression, is observed in materials like $In_{0.53}Ga_{0.47}As$

lattice-matched to InP substrates³⁹. The same situation can be observed in $HgCdTe$ ternary alloys⁴⁰. Consequence of enhancement in the radiative lifetime leads to higher ultimate performance of photodiodes. Assuming the same situation for SWIR $HgCdTe$ photodiodes, Rogalski and Ciupa have reconsidered the ultimate performance of P -on- n $HgCdTe$ photodiodes and compared theoretical predictions with attainable experimental data, as shown in Fig. 12. We can see that SWIR $HgCdTe$ photodiodes have good performance over a wider range of wavelengths⁴¹. It is due to lattice match of active base photodiode layers with $CdZnTe$ substrate, and consequently negligible influence of induced defects at interface on photodiode leakage current.

Figure 13 shows the detectivity as a function of temperature for $HgCdTe$ FPAs at various cut-off wavelengths and operating background. In nearly all cases, the performance is characterised by BLIP,

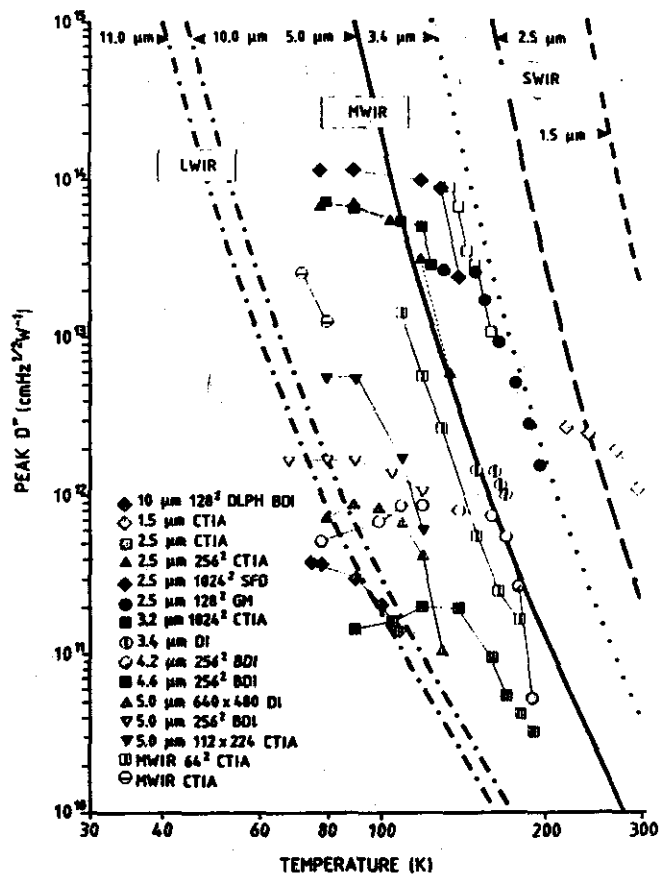


Figure 13. Detectivity of $HgCdTe$ FPAs versus temperature

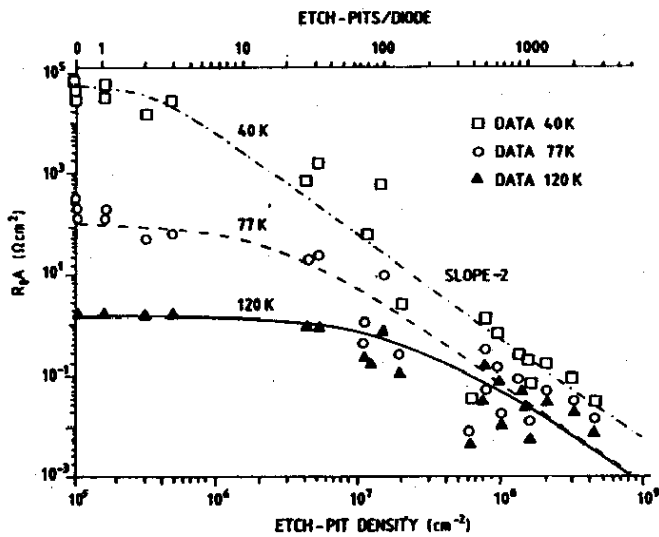


Figure 14. R_0A product versus EPD, showing fit of model to data for 9.5 μm array (at 78K), measured at 120K, 77K, and 40K at zero FOV.

transitioning to detector-limited performance as the temperature is increased.

5. SOURCES OF DARK CURRENT OF *HgCdTe* PHOTODIODES

Many excess mechanisms are involved in determining the dark current of *HgCdTe* photodiode^{12, 42}. Apart from the fundamental band-to-band generation in the base region, additional contributions may arise from non-fundamental sources due to the base and cap layer, depletion region and surface. As the photodiode operating temperature is lowered, the thermal dark current mechanisms become weaker and allow other mechanisms to prevail. In practice, the non-fundamental sources dominate the dark current of the present *HgCdTe* photodiodes, with the exception of specific cases of near-room temperature devices and highest quality 77K LWIR and 200K MWIR devices. The main leakage mechanisms of *HgCdTe* photodiodes are: Generation in the depletion region, interband tunnelling, trap-assisted tunnelling, and impact ionisation. Some of these are caused by structural defects in the *p-n* junction. These mechanisms are receiving much attention now, particularly because they determine ultimately the array uniformity,

yield and cost for some applications, particularly those with lower operating temperatures.

Many researchers have successfully modelled the key reverse bias leakage mechanism in LWIR *HgCdTe* photodiodes at $\leq 77\text{K}$ in terms of trap-assisted tunnelling⁴². The role played by traps in the depletion region is very complicated. Nemirovsky⁴³, *et al.* have shown that, for gold-doped material, the observed temperature and voltage behaviour of the current-voltage characteristic fits a trap-assisted tunnelling model below 100K, and at biases over -80 mV . DeWames⁴⁴, *et al.* have shown that a model based on a thermal-tunnel process can explain the bias-dependent behaviour of reverse current in long-wavelength diodes. Also, Nemirovsky⁴⁵, *et al.* have explained the observed properties of their *n⁺-p* junctions by a thermal trap-assisted tunnelling process, modelled for the special case of the trap residing at the Fermi level.

Dislocations are known to increase dark current and $1/f$ noise current. The reverse bias characteristics of *HgCdTe* diodes depend strongly on the density of dislocations intercepting the junction. Johnson⁴⁶, *et al.* showed that for large dislocation density, the R_0A product decreases as the square of the dislocation density; the onset of the square dependence occurs at progressively lower dislocation densities as the temperature decreases, as shown in Fig. 14. At 77K, R_0A begins to decrease at an etch-pit-density (EPD) of approximately 10^6 cm^{-2} , while at 40K, R_0A is immediately affected by the presence of one or more dislocations in a diode. The scatter in the R_0A data at large EPD may be associated with the presence of an increased number of pairs of interacting dislocations being present in some of those diodes; these pairs are more effective in reducing the R_0A than individual dislocations. The dependence of the detector R_0A product on dislocation density is explained by a phenomenological model based on the conductances of individual and interacting dislocations which shunt the *p-n* junction. Spectral response and quantum efficiency are only weakly

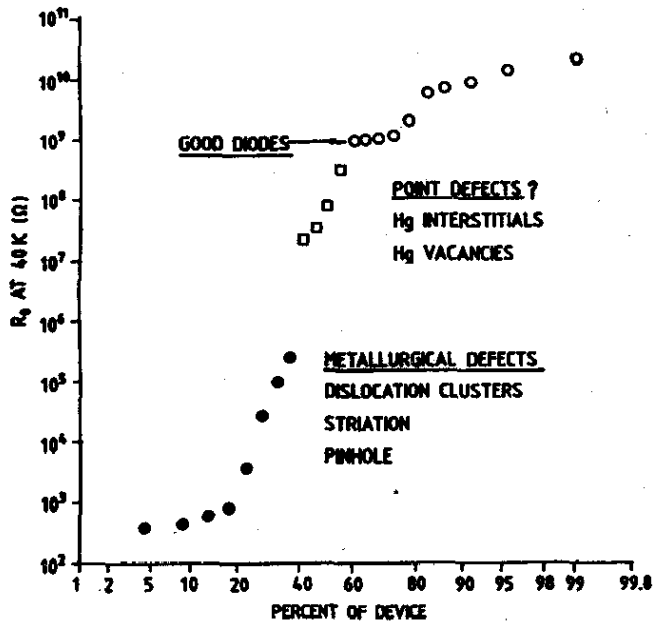


Figure 15. Detailed analysis separates the cumulative distribution function of R_0A values of LWIR p -on- n $HgCdTe$ photodiodes (fabricated by LPE) into three regions: Good diodes, diodes affected by point defects, and diodes affected by metallurgical defects.

affected. Instead, the $1/f$ noise current was found to increase approximately linearly with dislocation density.

For low background applications, the $HgCdTe$ photodiodes are operated at 40K. The R_0A product distribution for P -on- n DLHJ devices at this temperature spans a wide range of several orders of magnitude. Chen⁴⁷, *et al.* carried out a detailed analysis of the wide distribution of the R_0 values. Figure 15 shows the cumulative distribution functions of R_0 values at 40K from devices with a cut-off wavelength between 9.4 μm and 10.5 μm . It is clear that while some devices exhibit a fair operability with R_0 values spanning only two orders of magnitude, other devices show a poor operability with R_0 values spanning > 5 -6 orders of magnitude. Lower performance, with R_0 values $< 7 \times 10^6 \Omega$ at 40K, usually contained gross metallurgical defects, such as dislocation clusters and loops, pinholes, striations, telluride inclusions, and heavy terracing. However, diodes with R_0 values between $7 \times 10^6 \Omega$ and $1 \times 10^9 \Omega$ at 40K contained no visible defects (mercury interstitials and vacancies). Dislocations,

twins and sub-grain boundaries in LWIR n^+p $HgCdTe$ photodiodes primarily produce bias-dependent dark current, while tellurium precipitation and associated dislocation multiplication produces bias-dependent noise⁴⁸.

6. DUAL-BAND $HgCdTe$ DETECTORS

Multicolour capabilities are highly desirable for advance IR systems. Systems that gather data in separate IR spectral bands can discriminate both absolute temperature and unique signatures of objects in the scene. By providing this new dimension of contrast, multiband detection also enables advanced colour processing algorithms to further improve sensitivity above that of single-colour devices. This is important for identifying temperature difference between missile target, warheads and decoys. Multispectral IR FPAs can also play many important roles in Earth and planetary remote sensing, astronomy, etc. It is expected that four colours may be about the limiting number of bands that can be stacked in a single pixels¹. For applications desiring greater spectral decomposition, alternative approaches are being developed.

Currently, multispectral systems rely on cumbersome imaging techniques that either disperse the optical signal across multiple IR FPAs or use a filter wheel to spectrally discriminate the image focused on a single FPA. Also complex alignment is required to map the multispectral image, pixel-to-pixel. Consequently, these approaches are expensive in terms of size, complexity, and cooling requirements.

Both $HgCdTe$ photodiodes and QWIPs offer the multicolour capability in the MWIR and LWIR range. Each of these technologies has its advantages and disadvantages. QWIP technology is based on the well-developed A^3B^5 material system which has a large industrial base with a number of military and commercial applications. $HgCdTe$ material system is only used for detector applications. Therefore, QWIPs are easier to fabricate with high yield, high operability, good uniformity and lower cost. On the other hand, $HgCdTe$ FPAs have higher quantum

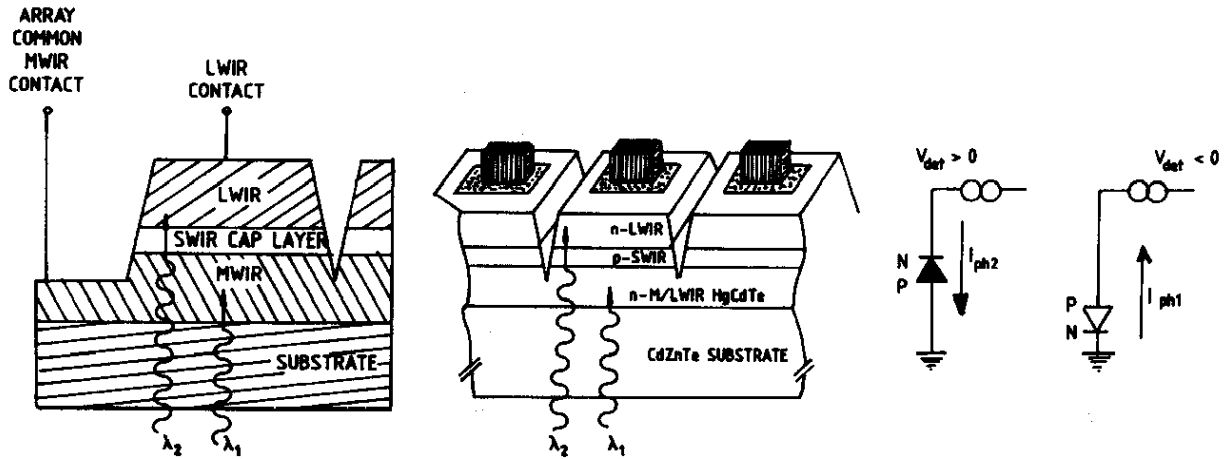


Figure 16. Cross-section of integrated two-colour detectors in an *n-P-N* layer structure for sequential operating mode

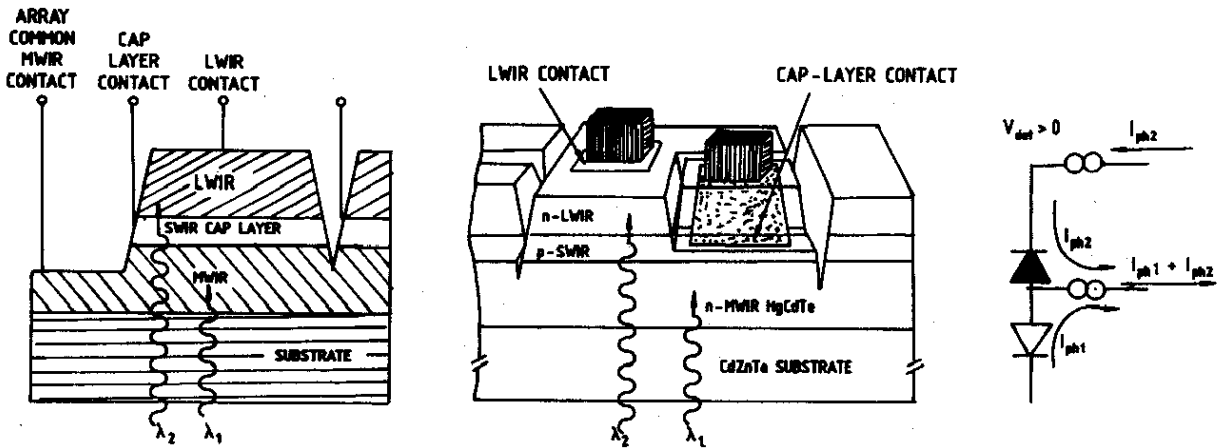


Figure 17. Cross-section of integrated two-colour detectors in an *n-P-N* layer structure for simultaneous operating mode

efficiency, higher operating temperature and potential for the highest performance. A detailed comparison of both technologies has been recently given by Tidrow⁴⁹, *et al.* and Rogalski⁵⁰.

Integrated two-colour technology *HgCdTe* has been developed for nearly a decade with a steady progression having a wide variety of pixel size (30 μm to 61 μm), array formats (64 \times 64 up to 320 \times 240) and spectral-band sensitivity (MWIR/MWIR, MWIR/LWIR and LWIR/LWIR). Following the successful demonstration of multispectral detectors in LPE-grown *HgCdTe* devices, the MBE and MOCVD techniques have been used for the growth of a variety of multispectral detectors. Considerable progress has been achieved, especially by research groups at Raytheon^{51,52} and Lockheed Martin^{53,54} employing

MBE and MOCVD techniques for the growth of variety devices.

The two-colour detector arrays are based on an *n-P-N HgCdTe* triple-layer heterojunction (TLHJ) design (Figs 16 and 17). TLHJ detectors consist of back-to-back photovoltaic *p-n* junctions. Radiation for both bands is incident on the shorter band detector, with the LW radiation passing through the second detector. This device architecture is realised by placing a LW *HgCdTe* photodiode simply behind SW photodiode. It should be noticed that also an *n-p-p-p-n* structure has been demonstrated in which ion implantation was used to form a planar *p-on-n* photodiode in *p-p-p-n* films grown by MBE onto germanium structures⁵⁵.

Both the sequential mode and the simultaneous mode detectors are fabricated from the multilayer

materials. The mode of detection is determined by the fabrication process. The sequential mode detector (Fig. 16) has a single indium bump per unit cell that permits sequential bias selectivity of the spectral bands associated with operating tandem photodiodes. The simultaneous mode detector (Fig. 17) employs an additional electrical contact to the shared-type centre layer so that each junction can be accessed independently with both signal channels integrated simultaneously. The two indium bumps per unit cell required for the simultaneous mode detectors can be fabricated in relatively small unit cells with high optical fill factor.

Critical step in device formation is connected with *in situ* doped *p*-type arsenic-doped layer with good structural and electrical properties to prevent internal gain from generating spectral crosstalk. The band gap engineering effort consists of increasing the *CdTe* mole fraction and the effective thickness of the *p*-type layer to suppress out-of-band carriers from being collected at the terminals.

The problems with the bias-selectable device are: Its construction does not allow independent selection of the optimum bias voltage for each photodiode, and there can be substantial MW crosstalk in the LW detector. To overcome the problems of the bias-selectable device, the independently accessed back-to-back photodiode dual-band detectors have been proposed. An implementation of the simultaneous mode using a second indium bump in the unit cell is shown in Fig. 18. The mesa shape has become complicated to provide access to the cap layer for the third contact. Internal gain is effectively suppressed through proper bias of each diode, making the design and growth emphasis on band gap engineering easier. The most important distinction is the requirement of a second ROIC in each unit cell. LW band fill factor is reduced from that of the MW, since some junction area is sacrificed to provide contact to the buried cap layer, and spatial coincidence is altered. The difference between sequential and

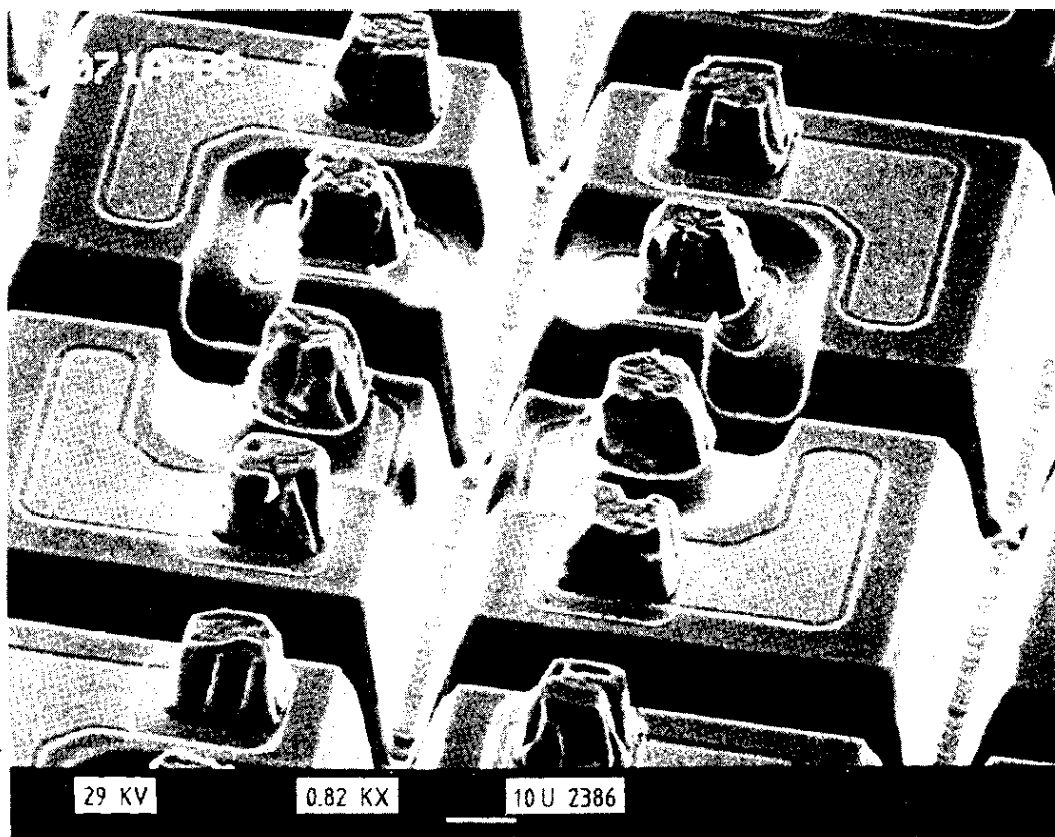


Figure 18. SEM photo of a 64 × 64 two-colour *HgCdTe* detector array with 75 µm × 75 µm unit cells

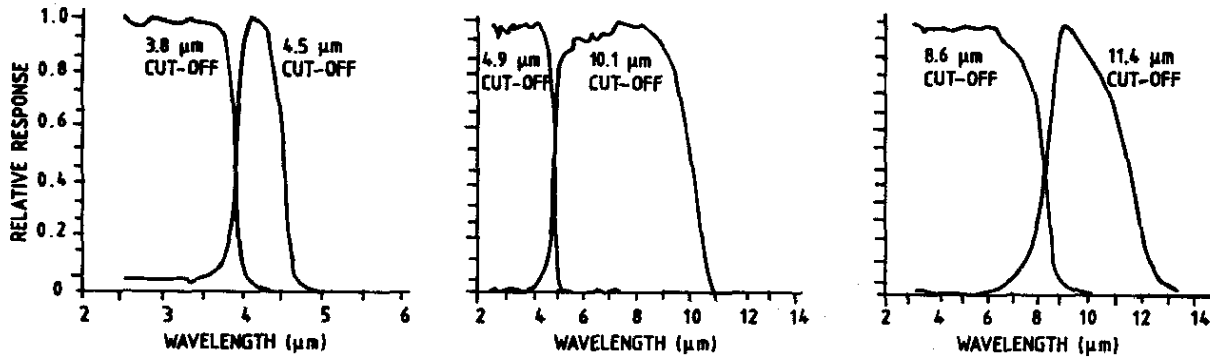


Figure 19. Spectral response curves for two-colour *HgCdTe* detectors in various dual-band combinations of spectral bands

simultaneous operation becomes to some extent, indistinct when two widely separated spectral bands such as 3 μm –5 μm and 10 μm –12 μm bands are used. Photon fluxes in the LW band are generally much higher than in the SW band, requiring a significantly shorter integration time for the LW band, and loss of true simultaneity of signal integration can occur. In this situation, a smaller LWIR fill factor can be a benefit in reducing background-generated charge.

One key technical issue in epi-grown two-colour *HgCdTe* detectors is high dislocation densities at the interfaces between adjacent layers⁵². Dual-band *HgCdTe* detectors are significantly thicker than single-colour ones and critical thicknesses can be exceeded resulting in misfit dislocations, which are not important in single-colour devices. Recently, a quaternary *HgCdZnTe* layer has been used to achieve better lattice matching and reduce misfit dislocations between adjacent layers of different band gap⁵⁶.

Integrated two-colour detectors have been implemented in a number of variations of structure and material for operation in both sequential and simultaneous mode. Figure 19 shows examples of spectral response from MWIR/MWIR, MWIR/LWIR, and LWIR/LWIR two-colour devices. Note that there is a minimal crosstalk between the bands, since the SW band absorbs nearly 100 per cent of the SWs. Test structure indicates that separate photodiodes in a two-colour MWIR/MWIR detector perform exactly as single-colour detectors in terms of achievable R_0A

product variation with wavelength at a given temperature.

Fill factors of 128 \times 128 MWIR/MWIR FPAs as high as 80 per cent were achieved using a single mesa structure to accommodate two indium bump contacts required for each unit cell with 50 μm size. The bottom *n*-type layer served as the common ground. Quantum efficiencies of 70 per cent were observed in 2.5 μm –3.9 μm and 3.9 μm –4.6 μm bands without using an anti-reflection coating. The R_0A values for the diodes ranged⁵² from $8.25 \times 10^5 \Omega\text{cm}^2$ to $1.1 \times 10^6 \Omega\text{cm}^2$ at $f/2$ FOV. NEDT for both bands was below 25 mK (Fig. 20) and imagery was acquired at 180K with no visible degradation in image quality. The camera used for these measurements had a 50 mm, $f/2.3$ lens.

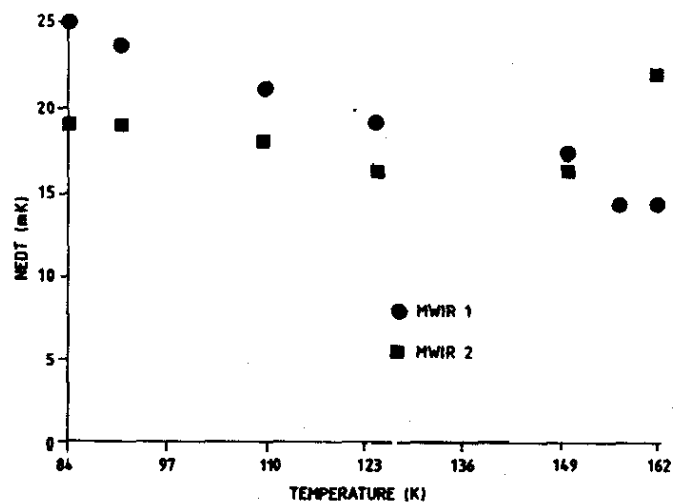


Figure 20. NEDT for two-colour camera having 50 mm, $f/2.3$ lens, as a function of operating temperature.

The experimentally demonstrated⁵⁴ 64 × 64 MW/LW dual-band MOCVD FPAs have a unit cell (75 μm × 75 μm). These arrays were hybridised to a dual-band silicon multiplexer ROIC that allowed the MW and LW photocurrents to be integrated simultaneously and independently. These staring arrays exhibit high average quantum efficiency (MW: 79 per cent; LW: 67 per cent), high median detectivities (MW: 4.8 × 10¹¹ cm Hz^{1/2}W⁻¹; LW: 7.1 × 10¹⁰ cm Hz^{1/2}W⁻¹), and low median NEDTs (MW: 20 mK; LW: 7.5 mK for T_{SCENE} = 295K and f/2.9).

7. ANTICIPATED EVOLUTION OF IR TECHNOLOGY

The future applications of IR detector systems require:

- Higher pixel sensitivity
- Further increases in pixel density to above 10⁶ pixels,
- Cost reduction in IR imaging array systems using less cooling sensor technology combined with integration of detectors and signal processing functions (with more on-chip signal processing)

- Improvements in the functionality of IR imaging arrays through development of multispectral sensors.

The research activity has been directed towards 2-D staring array detectors consisting of more than 10⁶ elements. The thermal detectors, which are relative newcomers, are narrowing the gap with photon detectors in respect of numbers of detectors per chip. IR FPAs have nominally the same growth rate as dynamic random access memory (RAM) integrated circuits (ICs) (which have had a doubling rate approximately 18 months; it is a consequence of Moore's law, which predicts the ability to double transistor integration on each IC about every 18 months) but lag behind by about 5–10 years. ROICs are somewhat analogous to dynamic RAM – only ROICs require a minimum of three transistors per pixel compared to one per memory cell. ROICs are also analogous with an emphasis on low-noise inputs and generally maximum charge storage capacity. Over the last decade, dramatic improvements in detector and ROIC technology have resulted in a 200 times increase in the size of

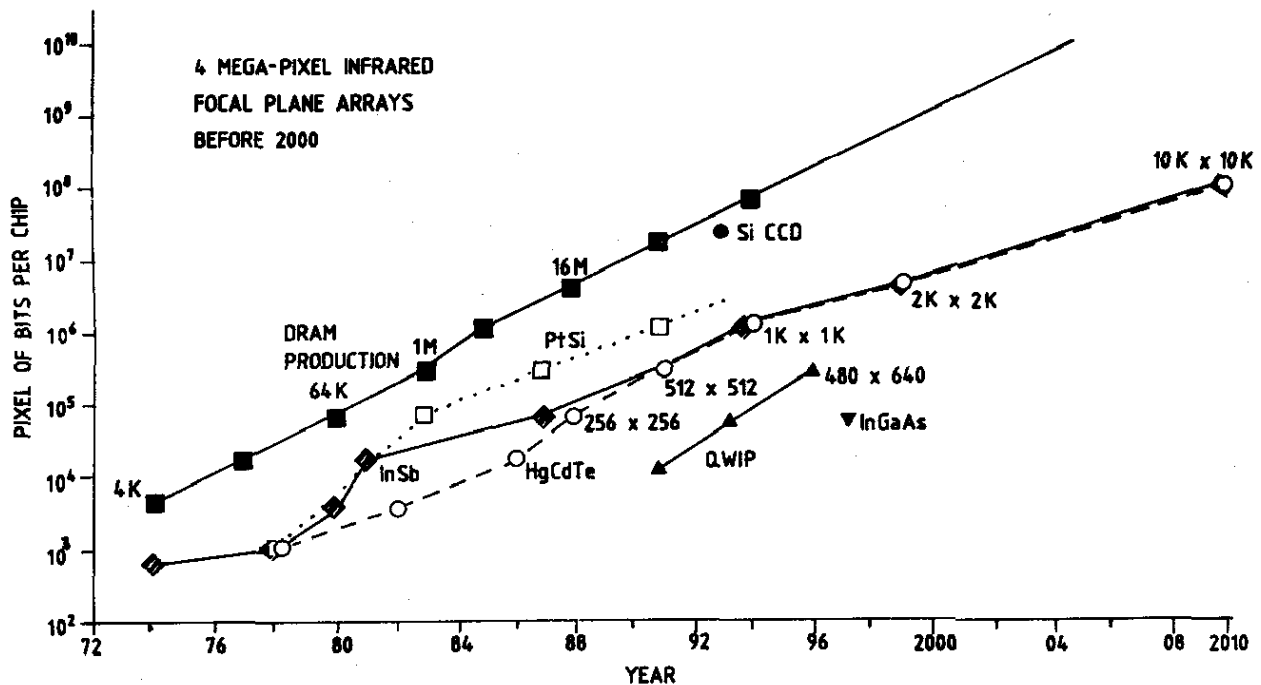


Figure 21. Increase in array format size over the past 25 years and projections for the coming decade. PtSi, InSb, and HgCdTe have been following the pace of dynamic RAM, offset by about a decade. QWIP detectors have been recently reported as large as 640 × 480 pixels.

the largest FPAs. Consequently, through various 64×64 FPAs were available in the early 1980s, several vendors are now producing monolithic FPAs in the TV-compatible 1040×1040 formats. Figure 21 illustrates the trend of array size over the past 25 years and some projections of what will evolve in the coming decade. Rockwell has developed the world's largest *HgCdTe* SWIR FPAs for astronomy and low background applications²⁹. The format of the device is a hybrid 2048×2048 with a unit cell ($18 \mu\text{m} \times 18 \mu\text{m}$).

CMOS multiplexers are the best choice to perform the integration and signal processing for 2-D arrays. CMOS-based imagers offer practical advantages wrt on-chip integration of camera functions, including command and control electronics, digitisation and image processing. On comparison with CCDs, the MOS multiplexers are characterised by high circuit density, fewer drive voltages, fewer clocks, much lower voltages and packing density compatible with many more special

functions. The advantages of CMOS are that existing foundries fabricate application specific integrated circuits (ASICs) that can be readily used by adapting their design rules. As a result, CMOS is now suitable also for TDI-type multiplexers. Design rules of $0.25 \mu\text{m}$ are in production with preproduction runs of the $0.18 \mu\text{m}$ design rules. Due to the availability of such fine design rules, more functionality has been put into the unit cells of IR and visible multiplexers and smaller unit cells, leading to large array sizes. Figure 22 shows the timelines for minimum circuit feature and the resulting CCD, IR FPA and CMOS visible imager sizes wrt imaging pixels. Also along the horizontal axis is a scale depicting the general availability of various MOS and CMOS processes. The ongoing migration to even finer lithographies will thus enable the rapid development of CMOS-based imagers having even higher resolution, better image quality, higher levels of integration and lower overall imaging system cost than CCD-based

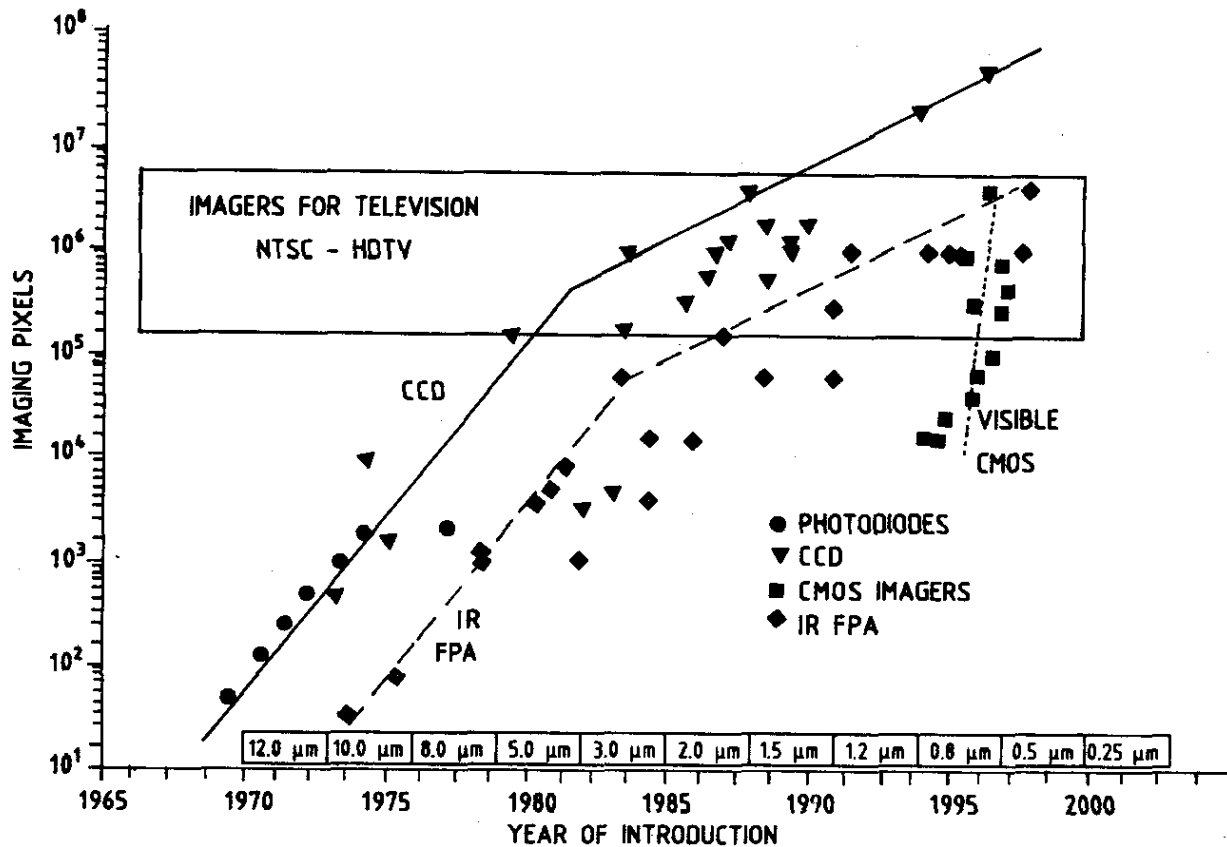


Figure 22. Chronology of imager pixel count (CCD, IR FPA and CMOS). The timeline design rules are shown at the bottom.

solutions. At present, CMOS with minimum feature $\leq 0.5 \mu\text{m}$ is also enabling monolithic visible CMOS imagers, because the denser photolithography allows low noise signal extraction and high performance detection with high optical fill factor within each pixel⁵⁷. The silicon wafer production infrastructure which has put PCs into many homes is now enabling CMOS-based imaging in consumer products, such as video and digital still cameras.

To reduce the real cost of the IR image systems, one must take action on all the elements which make up the cost. The cost can be broken down into three parts: The chip (detector + ROIC), the dewar, and integration and tests. The user must add the cryogenic machine cost that is not negligible compared to that of the cost of the component. This explains why the cost of *PtSi* or QWIPs is not markedly less than that of photon detectors of the same complexity, even though the raw materials (silicon and *GaAs*) is much less than for *HgCdTe*. In addition, since *PtSi* requires a very wide optical aperture to obtain acceptable performance, and since QWIP requires a lower operating temperature than the other photon detectors, a possible reduction in the purchase price is counterbalanced by a significant increase in operating costs⁵⁸.

Detector maturity is a function of the accumulated experience and development effort, the complexity of the device required, and the inherent difficulty presented by the material technology. At present, *HgCdTe* photodiodes and blocked impurity band (BIB) extrinsic silicon detectors are not fully mature. *PtSi* technology is mature and has attained a plateau. Other two detector technologies, such as *InSb* and silicon bolometers are still evolving significantly as applications for larger array configurations and smaller pixel sizes continue to push the technology. Other mature technologies, such as *PbS*, *PbSe* and *HgCdTe* photoconductors have significant enhancement in their performance in the last three decades in response to demands for higher responsivity, lower $1/f$ noise, better uniformity, and greater producibility.

Thermal detector arrays will increase in size and improve in thermal sensitivity to a level satisfying high performance applications at ambient temperature. It is supposed that the silicon microbolometer arrays and the monolithic pyroelectric arrays will capture the low-cost markets. Current uncooled bolometer FPAs have achieved NEDT $< 10 \text{ mK}$ with $f/1$ optics, that has opened the door to the use of less expensive slower optical systems. Generally in comparison with photon detectors, the performance of thermal detector is modest, these suffer from slow response, and they not very useful in application requiring multispectral detection.

At present, Cadillac 2000 car model offers an IR imaging system based on Texas Instruments pyroelectric 240×320 hybrid FPAs⁵⁹. Within a decade, such systems will be standard equipment on luxury cars and optional equipment on almost all car models. IR imagery gives the driver an ability to see several times further ahead than with headlights and the relative distance advantage will probably be even greater under some weather conditions, such as fog. It is supposed that sale of IR imaging equipment to the automobile market will begin to rapidly change the relative ratio between military/government and commercial IR markets. Today, only about 10 per cent of the market is commercial. After a decade, the commercial market can grow to over 70 per cent in volume and 40 per cent in value, largely connected with volume production of uncooled imagers for automobile driving. In large volume production for automobiles' drivers, the cost of uncooled imaging systems will decrease to $< \$1000$. Of course, these systems will cover other segments of the transportation industry: Trucks, trains, ships, barges and buses. The cheapest uncooled IR imagers will be deployed for everyday tasks, including amusement. Perhaps microelectromechanical structures (MEMs) technology will allow to be developed as direct-view sensors which can be used like optical binoculars.

The main drawback of uncooled thermal detectors is their slow response. For some

applications requiring uncooled detectors, the slow response is unacceptable. Recently, a number of concepts (e.g. nonequilibrium device,⁹ multijunction *HgCdTe* photodiodes,⁶⁰ optical immersion) and new materials (*InAs/GaSb*-based type II superlattices) have been proposed to improve performance of photon detectors operating at near room temperature. The measurements show the possibility to achieve detectivity⁶¹ of $\approx 1 \times 10^9$ cmHz^{1/2}/W at the 8–9 μm range and potentially, the devices can be assembled in large FPAs⁶¹. These possibilities will outperform the present-day performance of uncooled thermal detectors.

Despite serious competition from alternative technologies and slower progress than expected, *HgCdTe* is unlikely to be seriously challenged for high performance applications, applications requiring multispectral capability and fast response. The recent successes of competing cryogenically cooled detectors are due to technological, not fundamental issues. There are good reasons to think that the steady progress in epitaxial technology would make *HgCdTe* devices more affordable in the near future. The much higher operation temperature of *HgCdTe*, compared to Schottky barrier devices and low dimensional solid devices, may become a decisive argument in this case.

The fundamental performance limits of *HgCdTe* photodiodes have not been reached yet. Further progress will be in direct proportion to the effort directed toward basic materials science and processing technology. Continued development of the *in situ* vapour phase epitaxy methods (MBE and MOCVD) will allow band gap engineering heterojunction devices of improved quality and increasing complexity. Also, continued development of epitaxial growth on alternative substrates such as silicon will reduce the cost of 2-D arrays. SWIR arrays will be developed for starlight imaging applications in the 1.0 μm –2.5 μm region. Efforts to extend the useful cut-off wavelength to beyond the present 17 μm will continue. Higher operating temperature will continue to receive attention, through reduction of Shockley-Read

defects and unique device heterostructures. Development of dual-band arrays will continue and three-band detectors will soon be demonstrated. To provide high resolution spectroscopic imaging, larger *HgCdTe* FPAs will be used in Fourier-transform interferometers. Photodiodes will replace photoresistors for detection to 15 μm since these are characterised by more linear response.

The situation concerning QW structures and SLs is not clear; however, unique detection capabilities may arise from the low dimensional solids. Situation of LWIR QWIPs is clear. The initial results show promise for the growth of QWIPs on silicon wafers and applications for integration with silicon-based electronics⁶². It is expected that the QWIP hand-held, and cost-effective cameras will find imaging and spectroscopy applications in LWIR spectral band. Powerful possibilities of QWIP technology are connected with VLWIR FPA applications and with multicolour detection. Three-band and four-band FPAs will be developed in near future.

Finally, considerable development of signal processing function into FPAs can be anticipated. Today, many devices have digital programming interfaces to control read-out operation (integration, scan direction, gain adjustment, etc.). The next few years will see that on-chip analogue-to-digital conversion becomes commonplace, followed by non-uniformity correction.

ACKNOWLEDGEMENT

This work was partially supported by the Polish State Committee for Scientific Research (Poland) under grant number PBZ 28.11/P6.

REFERENCES

1. Norton, P.R.. Infrared detectors in the next millennium. *Proceedings. SPIE*, 1999, **3698**, 652–65.
2. Lawson, W. D.; Nielson, S.; Putley, E. H. & Young, A. S. Preparation and properties of *HgTe* and mixed crystals of *HgTe-CdTe*. *J. Phys. Chem. Solids*, 1959, **9**, 325–29.

3. Kruse, P.W. & Pickenpaugh, T.D. Air Force Technical Monitor, U.S. Air Force Contract AF33(616)-7901. Honeywell Research Center, Hopkins, Minnesota.
4. Kruse, P.W.; Blue, M.D.; Garfunkel, J.H. & Saur, W.D. Long wavelength photoeffects in mercury selenide, mercury telluride and mercury telluride-cadmium telluride. *Infrared Phys.*, 1962, 2, 53.
5. Rogalski, A. *Infrared Detectors*. Gordon and Breach, London, 2000.
6. Piotrowski, J. & Gawron, W. Ultimate performance of infrared photodetectors and figure of merit of detector material. *Infrared Phys. Technol.* 1997, 38, 63-68.
7. Rogalski, A. New Ternary Alloy Systems for Infrared Detectors. SPIE Optical Engineering Press, Bellingham, 1994.
8. Johnson, J.L. The *InAs/GaInSb* strained layer superlattice as an infrared detector material: An overview, *Proceedings SPIE*.
9. Elliott, T. New infrared and other applications of narrow gap semiconductors. *Proceedings SPIE*, 1998, 3436, 763-75.
10. Rogalski, A. Comparison of the performance of quantum well and conventional bulk infrared photodetectors. *Infrared Phys. Technol.*, 1997, 38, 295-10.
11. Vural, K.; Kozlowski, L.J.; Cooper, D.E.; Chen, C.A.; Bostrup, G.; Cabelli, C.; Arias, J.M.; Bajaj, J.; Hodapp, K.W.; Hall, D.N.B.; Kleinhans, W.E.; Price, G.G. & Pinter, J.A. 2048 × 2048 *HgCdTe* focal plane arrays for astronomy applications. *Proceedings SPIE*, 3698, 1999, 24-35.
12. Reine, M.B. Photovoltaic detectors in *HgCdTe*, *In Infrared detectors and emitters: Materials and devices*, edited by P. Capper and C.T. Elliott. Chapman and Hall, London, 2000.
13. Rodot, M.; Verie, C.; Marfaing, Y.; Besson, J. & Lebloch, H. Semiconductor lasers and fast detectors in the infrared (3 to 15 μm). *IEEE J. Quant. Electron.* 1966, 2, 586-93.
14. Melngailis, I.; Keicher, W.E.; Freed, C.; Marcus, S.; Edwards, B.E.; Sanchez, A.; Yee, T. & Spears, D.L. Laser radar component technology. *Proceedings IEEE*, 1996, 84, 227-67.
15. Cohen-Solal, G.D. & Lussereau, A.G. US Patent 3, 988, 774.1976.
16. *Infrared detectors – product profile*. GEC-Marconi Infra-Red Limited, 1997.
17. Turner, A.; Teherani, T.; Ehmke, J.; Pettitt, C.; Conlon, P.; Beck, J.; McCormack, K.; Colombo, L.; Lahutsky, T.; Murphy, T. & Williams, B. Producibility of VIPTM scanning focal plane arrays. *Proceedings SPIE* 1994, 2228, 237-48.
18. Bubulac, L.O. & Tennant, W.E. Role of Hg in junction formation in ion-implanted *HgCdTe*. *Appl. Phys. Lett.*, 1987, 51, 355-57.
19. Destefanis, G. & Chamonal, J.P. Large improvement in *HgCdTe* photovoltaic detector performances at LETI. *J. Electron. Mater.*, 1993, 22, 1027-32.
20. Rogalski, A. & Ciupa, R. Theoretical modeling of long wavelength *n⁺-on-p HgCdTe* photodiodes. *J. Appl. Phys.*, 1996, 80, 2483-489.
21. Ashley, T. & Elliott, C.T. Non-equilibrium mode of operation for infrared detection. *Electron. Letters*, 1985, 21, 451-52.
22. Ashley, T.; Elliott, T.C & White, A.M. Non-equilibrium devices for infrared detection. *Proceedings SPIE*, 1985, 572, 123-32.
23. Tobin, S.P.; Weiler, M.H.; Hutchins, M.A.; Parodos, T. & Norton, P.W. Advances in composition control for 16 μm LPE *p-on-n HgCdTe* heterojunction photodiodes for remote sensing applications at 60 K. *J. Electron. Mater.*, 1999, 28, 596-02.
24. Arias, J.M.; Pasko, J.G.; Zandian, M.; Kozlowski, L.J. & DeWames, R.E. Molecular beam epitaxy *HgCdTe* infrared photovoltaic detectors. *Optical Engineering*, 1994, 33, 1422-428.

25. Tennant, W.E.; Cockrum, C.A.; Gilpin, J.B.; Kinch, M.A.; Reine, M.B. & Ruth, R.P. Key issues in *HgCdTe*-based focal plane arrays: a industry perspective. *J. Vac. Sci. Technol.*, 1992, **B10**, 1359-369.
26. Tung, T.; DeArmond, L.V.; Herald, R.F.; Herning, P.E.; Kalisher, M.H.; Olson, D.A.; Risser, R.F.; Stevens, A.P. & Tighe, S.J. State-of-the-art of *Hg*-melt LPE *HgCdTe* at Santa Barbara Research Center. *Proceedings SPIE*, 1992, **1735**, 109-34.
27. de Lyon, T.J.; Rajavel, R.D.; Jensen, J.E.; Wu, O.K.; Johnson, S.M.; Cockrum, C.A. & Venzor, G.M. Heteroepitaxy of *HgCdTe*(112) infrared detector structures on *Si*(112) substrates by molecular-beam epitaxy. *J. Electron. Mater.*, 1996, **25**, 1341-346.
28. Wijewarnasuriya, P.S.; Zandian, M.; Edwall, D.D.; McLevige, M.V.; Chen, C.A.; Pasko, J.G.; Hildebrandt, H.; Chen, A.C.; Arias, J.M.; D'Souza, A.I.; Rujirawat, S. & Sivananthan, S. MBE *p-on-n Hg_{1-x}Cd_xTe* heterostructure detectors on silicon substrates. *J. Electron. Mater.*, 1998, **27**, 546-49.
29. Rogalski, A. Heterostructure infrared photovoltaic detectors. *Infrared Phys. Technol.*, 2000, **41**, 213-38.
30. Piotrowski, J.; Galus, W. & M. Grudzien', Near-room temperature IR photodetectors. *Infrared Physics*, **31**, 1-48.
31. Johnson, S.M.; de Lyon, T.J.; Cockrum, C.A.; Hamilton, W.J.; Tung, T.; Gesswein, F.I.; Baumgratz, B.A.; Ruzicka, L.M.; Wu, O.K. & Torh, J.A. Direct growth of *CdZnTe/Si* substrates for large-area *HgCdTe* infrared focal plane arrays. *J. Electron Mater.*, 1995, **24**, 467-73.
32. Vural, K. Mercury cadmium telluride short- and medium-wavelength infrared staring focal plane arrays. *Optical Engineering*, 1987, **26**, 201-08.
33. Kozłowski, L.J.; Bailey, R.B.; Cabelli, S.A.; Cooper, D.E.; Gergis, I.S.; Chen, A.C.; McLevige, W.V.; Bostrup, G.L.; Vural, K.; Tennant, W.E.; P.H. Howard, High-performance 5 μm 640 \times 480 *HgCdTe*-on-sapphire focal plane arrays. *Optical Engineering*, 1994, **33**, 54-63.
34. Kozłowski, L.J. *HgCdTe* focal plane arrays for high performance infrared cameras. *Proceedings SPIE* **3179**, 1997, 200-11.
35. de Lyon, T.J.; Rajavel, R.D.; Vigil, J.A.; Jensen, J.E.; Wu, O.K.; Cockrum, C.A.; Johnson, S.M.; Venzor, G.M.; Bailey, S.L.; Kasai, I.; Ahlgren, W.L. & Smith, M.S. Molecular-beam epitaxial growth of *HgCdTe* infrared focal-plane arrays on silicon substrates for midwave infrared applications. *J. Electron. Mater.*, 1998, **27**, 550-55.
36. Kozłowski, L.J.; Vural, K.; Bui, D.Q.; Bailey, R.B.; Cooper, D.E. & Stephenson, D.M. Status and direction of PACE-1 *HgCdTe* FPAs for astronomy. *Proceedings SPIE*, 1993, **1946**, 148-60.
37. Kozłowski, L.J.; Vural, K.; Cabelli, S.C.; Chen, C.Y.; Cooper, D.E.; Bostrup, G.L.; Stephenson, D.M.; McLevige, W.L.; Bailey, R.B.; Hodapp, K.; Hall, D. & Kleinhans, W.E. 2.5 μm PACE-1 *HgCdTe* 1024 \times 1024 FPA for infrared astronomy. *Proceedings SPIE*, 1994, **2268**, 353-64.
38. Bubulac, L.O.; Tennant, W.E.; Pasko, J.G.; Kozłowski, L.J.; Zandian, M.E. Motamedi, DeWames, R.E.; Bajaj, J.; Nayar, N.; McLevige, W.V.; Gluck, N.S.; Melendes, R.; Cooper, D.E.; Edwall, D.D.; Arias, J.M. & Hall, R. High performance SWIR *HgCdTe* detector arrays. *J. Electron. Mater.*, 1997, **26**, 649-55.
39. Rogalski, A. & Ciupa, R. Performance limitation of short wavelength infrared *InGaAs* and *HgCdTe* photodiodes. *J. Electron. Mater.*, 1997, **28**, 630-36.
40. Humpreys, R.G. Radiative lifetime in semiconductors for infrared detection. *Infrared Physics*, 1986, **26**, 337-42.
41. Kozłowski, L.J. *HgCdTe* focal plane arrays for high performance infrared camera. *Proceedings SPIE*, 1997, **3179**, 200-11.
42. Rogalski, A.; Rutkowski, J. & Adamiec, K. Narrow Gap semiconductor photodiodes. SPIE Optical Engineering Press, Bellingham, 2000.

43. Nemirovsky, Y.; Rosenfeld, D.; Adar, R. & Kornfeld, A. Tunnelling and dark currents in *HgCdTe* photodiodes. *J. Vac. Sci. Technol.*, 1989, **A7**, 528-35.
44. DeWames, R.E.; Williams, G.M.; Pasko, J.G. & Vanderwyck, A.H.B. Current generation mechanisms in small band gap *HgCdTe* *p-n* junctions fabricated by ion implantation. *J. Cryst. Growth.*, 1988, **86**, 849-58.
45. Nemirovsky, Y. ; Fastow, R.; Meyassed, M. & Unikovsky, A. Trapping effects in *HgCdTe*, *J. Vac. Sci. Technol.*, 1991, **B9**, 1829-1839 ()
46. Johnson, S.M.; Rhiger, D.R.; Rosbeck, J.P.; Peterson, J.M.; Taylor, S.M. & Boyd, M.E. Effect of dislocations on the electrical and optical properties of long-wavelength infrared *HgCdTe* photovoltaic detectors. *J. Vac. Sci. Technol.*, 1992, **B10**, 1499-506.
47. Chen, M.C.; List, R.S.; Chandra, D.; Bevan, M.J.; Colombo, L. & Schaake, H.F. Key performance-limiting defects in *p-on-n HgCdTe* heterojunction infrared photodiodes. *J. Electron. Mater.*, 1996, **25**, 1375-82.
48. List, R.S.; Tregilgas, J.H.; Turner, A.M.; Beck, J.D. & Ehmke, J.C. Electrical effects of subgrain boundaries, twins, dislocations and *Te* precipitation on LWIR *HgCdTe* photodiode arrays. *Proceedings SPIE*, 1994, **2228**, 274-82.
49. Tidrow, M.Z.; Beck, W.A.; Clark, W.W.; H.K.; Pollehn, Little, J.W.; Dhar, N.K.; Leavitt, P.R.; Kennerly, S.W.; Beekman, D.W.; Goldberg, A.C. & Dyer, W.R. Device physics and focal plane array applications of QWIP and MCT. *Opto-Electron Rev.*, 1999, **7**, 283-96.
50. Rogalski, A. Assessment of *HgCdTe* photodiodes and quantum well infrared photoconductors for long wavelength focal plane arrays. *Infrared Phys. Technol.*, 1999, **40**, 279-94.
51. Rajavel, R.D.; Jamba, D.M.; Wu, O.K.; Jensen, J.E.; Wilson, J.A.; Patten, E.A.; Kosai, K.; Goetz, P.; Chapman, G.R. & Radford, W.A. High performance *HgCdTe* two-color infrared detectors grown by molecular beam epitaxy. *J. Cryst. Growth* , 1997, **175**, 653-58.
52. Rajavel, R.D.; Jamba, D.M.; Jensen, J.E.; Wu, O.K.; Wilson, J.A.; Johnson, J.L.; Patten, E.A.; Kasai, K.; Goetz, P.M. & Johnson, S.M. Molecular beam epitaxial growth and performance of *HgCdTe*-based simultaneous- mode two-color detectors. *J. Electron. Mater.*, 1998, **27**, 747-51.
53. Mitra, P.; Barnes, S.L.; Case, F.C.; Reine, M.B.; O'Dette, P.; Starr, R.; Hairston, A.; Kuhler, K.; Weiler, M.H. & Musicant, B.L. MOCVD of band gap-engineered *HgCdTe p-n-N-P* dual-band infrared detector arrays. *J. Electron. Mater.*, 1997, **26**, 482-87.
54. Reine, M.B.; Hairston, A.; O'Dette, P.; Tobin, S.P.; Smith, F.T.J.; Musicant, B.L.; Mitra, P. & Case, F.C. Simultaneous MW/LW dual-band MOCVD *HgCdTe* 64×64 FPAs. *Proceedings SPIE*, 1998, **3379**, 200-12.
55. Ferret, P.; Zanatta, J.P.; Hamelin, R.; Cremer, S.; Million, A.; Wolny, M. & Destefanis, G. *J. Electron. Mater.*, 2000, **29**.
56. Johnson, S.M.; Johnson, J.L.; Hamilton, W.J.; Patten, E.A.; Peterson, J.M.; Leonard, D.B.; Strand, T.A.; Durham, J.H.; Randall, V.K.; deLyon, T.J.; Jensen, J.E. & Gorwitz, M.D. *J. Electron. Mater.*, 2000, **29**.
57. Kozlowski, L.J. ; Vural, K.; Luo, J.; Tomasini, A.; Liu, T. & Kleinmans, W.E. Low-noise infrared and visible focal plane arrays. *Opto-Electron Rev.*, 1999, **7**, 259-69.
58. Bertrand, F.; Tissot, J.L. & Destefanis, G. Second-generation cooled infrared detectors. State-of-the-art and prospects. *In Physics of semiconductor devices*, edited by Vikram Kumar and S.K. Agarwal. Narosa Publishing House, New Delhi, 1988.
59. Hamit, F. Military infrared takes to the road: The Cadillac's oncoming night vision option. *Advanced Imaging*, 1998, **13**(10), 34-35.

60. Piotrowki, J.; Nowak, Z.; Antoszewski, J.; Musca, C.; Dell, J. & Faraone, L. A novel multi-heterojunction $HgCdTe$ long-wavelength infrared photovoltaic detector for operation under reduced cooling conditions. *Semicond. Sci. Technol.*, 1998, **13**, 1209-214.
61. Piotrowski, J.; Grudzień, M.; Nowak, Z.; Orman, Z.; Pawluczyk, J.; Romanis, M. & Gawron, W. Uncooled photovoltaic $Hg_{1-x}Cd_xTe$ LWIR detectors. *Proceedings SPIE*.
62. Sengupta, D.K.; Gunapala, S.D.; George, T.; Bandara, S.V.; Chang-Chien, C.N.; Leon, R.; Kayali, S.; Kuo, H.C.; Fang, W.; Liu, H.C. & Stillman, G.E. Comparison of intersubband $GaAs/AlGaAs$ multiple quantum well infrared photodetectors on $GaAs$ and $GaAs$ -on- Si substrates. *Proceedings SPIE*, 1998, **3379**, 410-22.